CHALMERS
UNIVERSITY OF TECHNOLOGY

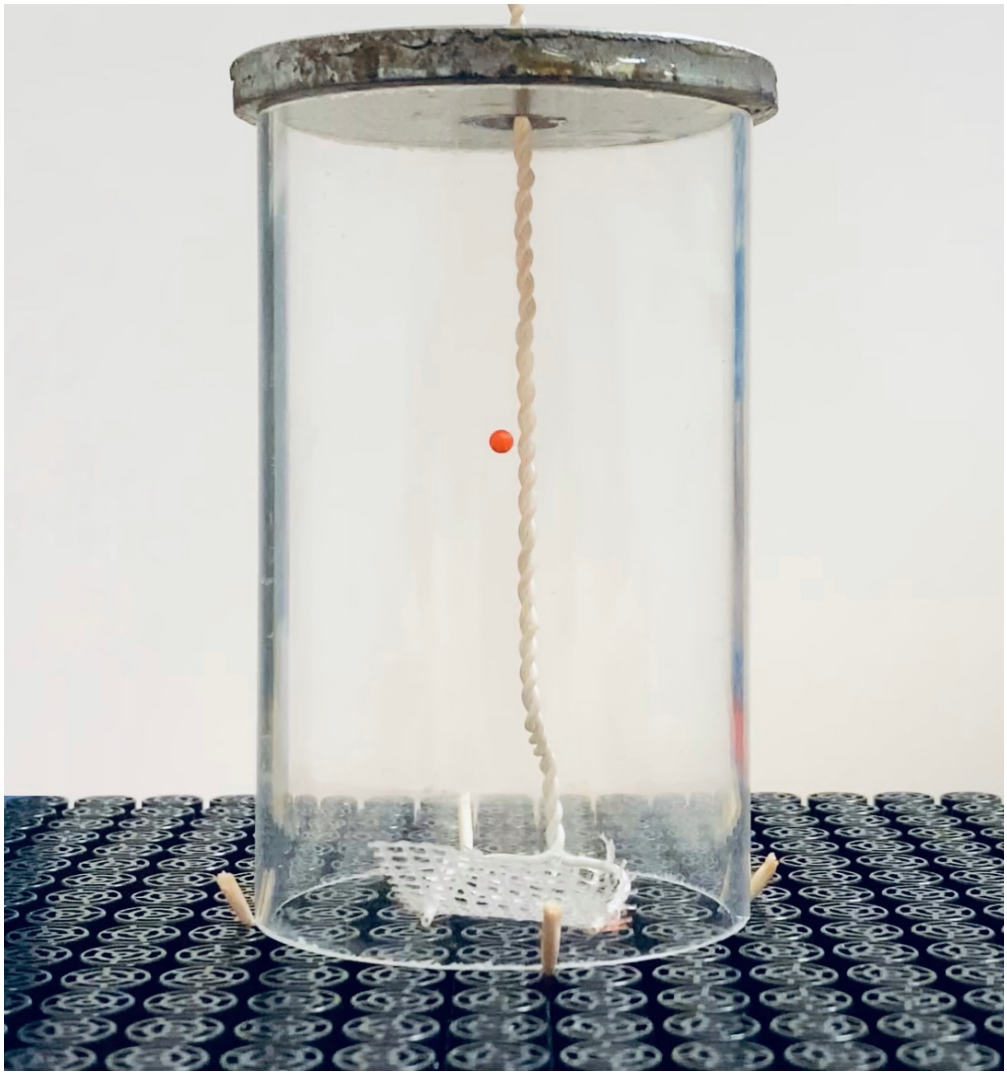

Acoustic Levitation in a Cylindrical Cavity

- a modal superposition approach

Master's thesis in Sound and Vibration

SIMON JOHANSSON

Division of Applied Acoustics
CHALMERS UNIVERSITY OF TECHNOLOGY
Gothenburg, Sweden 2021

Master's thesis ACEX30

Acoustic Levitation in a Cylindrical Cavity

- a modal superposition approach

SIMON JOHANSSON

CHALMERS
UNIVERSITY OF TECHNOLOGY

Department of Architecture and Civil Engineering
Division of Applied Acoustics
Chalmers University of Technology
Gothenburg, Sweden 2021

Acoustic Levitation in a Cylindrical Cavity
- a modal superposition approach
SIMON JOHANSSON

Supervisor: Carl Andersson, Division of Applied Acoustics
Examiner: Jens Ahrens, Division of Applied Acoustics

Master's Thesis ACEX30
Department of Architecture and Civil Engineering
Division of Applied Acoustics
Chalmers University of Technology
SE-412 96 Gothenburg
Telephone +46 31 772 1000

Cover: Bead levitated inside a cylindrical cavity.

Typeset in LaTeX
Printed by Chalmers Reproservice
Gothenburg, Sweden 2021

Acoustic Levitation in a Cylindrical Cavity
- a modal superposition approach
SIMON JOHANSSON
Division of Applied Acoustics
Chalmers University of Technology

Abstract

A method has been developed for calculating the acoustic radiation force acting on a small spherical bead in a sound field within a rigid boundary cylindrical cavity, using a modal approach. Modes are selected by a method comparing their relative strengths, within a specified dB range below the strongest mode. The total sound field is calculated as the superposition of fields from different excitation points, each composed of a summation of mode shapes within the specified range. The total sound field is then used to calculate the force, by use of a previously established model.

Three different simulated acoustic traps with a sound field excited by a plane transducer array at the bottom of the cylinder are presented. The traps are constructed by numerical optimization of the transducer phases and amplitudes such that the total sound field gives rise to converging forces at a designated position. One of the three simulated traps was also tested experimentally, where an acoustic trap at the designated position was not found. However, three other traps, one about 1 cm above the designated position, one in the center of the cylinder, and one about 5 mm offset from the center radially and in height, were found. Two of these alternate traps are also predicted by the developed model, which points towards the existence of a trap at the designated position as well, although hard to find by manual bead placement. The third found trap is not predicted by the model. Further research is needed to understand why that is, and how the model can be improved.

Keywords: Acoustic levitation, Cylindrical cavity, Modal superposition, Ultrasound, Phased array.

Contents

List of Figures

1 Introduction

Acoustic levitation is an emerging technology for suspending objects in a fluid (such as air) against the force of gravity, using only acoustic radiation forces, typically by use of sound in the ultrasonic range. For early setups this was done using the standing wave pattern created between a transducer and a reflecting surface, where small particles can be trapped at the nodes of the standing wave. In more recent years more complicated setups with arrays of multiple transducers are often used (although single transducer setups are still used in some applications for their simplicity). The wave pattern for levitation is then instead formed from the interference of sound fields from each transducer in the array. One big advantage of array setups is the ability to move the position of a trap in all three dimensions by manipulating the relative phases of the transducers.

There are many different kinds of transducer array setups, such as spatially focused arrays where all the transducers in the array are at the same distance from and directed at a single focus point, or plane arrays where the focusing of the sound field is achieved entirely by the relative phases between the transducers. There are single sided arrays where the sound field propagates in one direction, double sided setups creating standing waves in between two arrays opposite each other, and many more variations.

What most existing setups have in common is that the acoustic traps are generated in free field conditions, or with simple reflectors. Some research has been done on levitation in small cavities, for frequencies where the wavelength is comparable in size to the dimensions of the cavity, and strong resonances at isolated low order modes of the cavity are excited. There does not, however, seem to be as much previous research done on levitation in larger cavities, where superpositions of a wide range of higher order mode shapes have to be considered.

1.1 Related works

The theory for the acoustic radiation pressure on small spherical objects was first developed by King[1] in 1934, and was later generalized by Gor'kov[2] in 1962, into an expression for the potential of the acoustic radiation force. This Gor'kov potential formulation is valid for small spherical objects (much smaller than the acoustic wavelength at the frequency used) in acoustic fields consisting of plane and stationary waves, and is still in wide use today. This was further expanded upon by Sapozhnikov and Bailey[3] in 2012 to calculate the radiation force in an arbitrary acoustic field, including propagating fields such as those from a single sided transducer array.

Levitation between two opposite plane ultrasonic phased transducer arrays was demonstrated by Hoshi et al.[4] in 2014, with three-dimensional manipulation of trap positions. In 2015 Marzo et al.[5] achieved levitation using a single-sided transducer array. They also introduced a method for numerically optimizing the transducer phases to minimize the pressure amplitude and maximize the laplacian of the

Gor'kov potential at a designated position, thus constructing a trap. The advantage of using Sapozhnikov's expanded radiation force calculation, allowing for the inclusion of a term in the numerical optimization method for reducing rotational components of the force field, and thus increasing trap stability, was demonstrated by Carl Andersson and Jens Ahrens[6] in 2020.

In 1985 Barmatz and Collas[7] applied the method developed by Gor'kov to derive generalized potential and force expressions for arbitrary single mode standing waves within cylindrical as well as spherical and rectangular geometries. They investigated different possible acoustic trap positions with respect to isolated low order modes of the cavities. In 2019, Xu et al.[8] applied the same potential and force expressions for levitation of 2.5 µm radius polystyrene microspheres in a water filled cylindrical cavity with a height of 186 µm and a radius of 419 µm. Acoustic traps were constructed at different positions by simultaneously exciting two isolated modes, one purely axial mode to trap the spheres vertically, and one purely radial mode to trap them radially.

1.2 Aim

The aim of this thesis work is to investigate the possibility for levitation of small spherical beads within a cylindrical cavity. This report presents a method for constructing such acoustic traps, calculating the sound field from the standing wave shapes (modes) of the cavity, and numerically optimizing the transducer phases of a plane rectangular transducer array at the bottom off the cylinder, to produce an acoustic trap at a designated position.

2 Theory

2.1 Acoustic radiation force

The acoustic radiation force acting on an object arises from the change in wave momentum of the acoustic field when scattering off of the object. The force is obtained by integration of the wave momentum flux over a surface enclosing the object, averaged in time over the wave period. With a known incident field, the challenge is to determine the scattered field. Derivations for the scattered field from a small spherical object (i.e. $ka < 1$, where k is the wave number and a is the radius of the spherical object), as well as the force acting on it, have been presented by Sapozhnikov and Bailey[3], for an arbitrary incident field. This acoustic radiation force can be written as

$$\begin{aligned} F_\xi = -\frac{\pi}{\rho_0 c_0^2 k^5} \Re\Bigg\{ & ik^2 \Psi_0 p \frac{\partial p^*}{\partial \xi} + ik^2 \Psi_1 p^* \frac{\partial p}{\partial \xi} \\ & + 3i\Psi_1 \left(\frac{\partial p}{\partial x}\frac{\partial^2 p^*}{\partial x \partial \xi} + \frac{\partial p}{\partial y}\frac{\partial^2 p^*}{\partial y \partial \xi} + \frac{\partial p}{\partial z}\frac{\partial^2 p^*}{\partial z \partial \xi} \right) \Bigg\}, \end{aligned} \tag{2.1}$$

for each Cartesian coordinate direction $\xi = x, y, z$, where ρ_0 and c_0 are the density and the speed of sound, respectively, of the surrounding medium, and p is the sound pressure at the center of the spherical object. Ψ_0 and Ψ_1 are given by

$$\Psi_0 = -\frac{2(ka)^6}{9}\left(f_1^2 + \frac{1}{4}f_2^2 + f_1 f_2\right) - i\frac{(ka)^3}{3}(2f_1 + f_2) \tag{2.2}$$

$$\Psi_1 = -\frac{(ka)^6}{18}f_2^2 + i\frac{(ka)^3}{3}f_2 \tag{2.3}$$

$$f_1 = 1 - \frac{\rho_0 c_0^2}{\rho_* c_*^2} \tag{2.4}$$

$$f_2 = 2\frac{\rho_* - \rho_0}{2\rho_* + \rho_0}, \tag{2.5}$$

where a is the radius of the spherical object, and the constants f_1 and f_2 characterize the compressibility, $1/(\rho c^2)$, and density of the object in relation those of the surrounding medium. Properties of the object are denoted with a $*$ subscript.

In order to levitate an object at a point, $\mathbf{r}$, the total force exerted on it must be zero, with forces in a region around the point all converging towards it for stability. This can be stated mathematically as

$$\mathbf{F}(\mathbf{r}) + m\mathbf{G} = 0 \tag{2.6}$$

$$\frac{\partial F_x(\mathbf{r})}{\partial x} < 0 \qquad \frac{\partial F_y(\mathbf{r})}{\partial y} < 0 \qquad \frac{\partial F_z(\mathbf{r})}{\partial z} < 0, \tag{2.7}$$

where m is the mass off the object and $\mathbf{G}$ is the gravitational acceleration. These gradients have to be negative so that a positive displacement along any of the axes results in a negative, and thus restoring, force. This can be interpreted as the stiffness of the trap, where steeper slopes (more negative gradients) result in stronger restoring forces. The gradients of Equation 2.7 are referred to as the direct gradients throughout the rest of this report.

A further condition that the cross term gradients from the Jacobian of the force should be zero at the point can also be applied,

$$\begin{aligned} &\frac{\partial F_x(\mathbf{r})}{\partial y} = 0 \qquad \frac{\partial F_y(\mathbf{r})}{\partial x} = 0 \qquad \frac{\partial F_z(\mathbf{r})}{\partial x} = 0 \\ &\frac{\partial F_x(\mathbf{r})}{\partial z} = 0 \qquad \frac{\partial F_y(\mathbf{r})}{\partial z} = 0 \qquad \frac{\partial F_z(\mathbf{r})}{\partial y} = 0, \end{aligned} \tag{2.8}$$

which minimizes forces perpendicular to displacements from the trap position. A force field with strong cross term gradients (such as inwards spiralling force fields) may, even though it is convergent as a whole, send objects spiralling away from the trap due to their inertia.

2.2 Cylindrical modes

The pressure field inside a cavity is governed by the wave equation,

$$\frac{\partial^2 p}{\partial \rho^2} + \frac{1}{\rho}\frac{\partial p}{\partial \rho} + \frac{1}{\rho^2}\frac{\partial^2 p}{\partial \theta^2} + \frac{\partial^2 p}{\partial z^2} + k^2 p = 0, \tag{2.9}$$

here written in cylindrical coordinates. Within a cylindrical cavity of radius b and height h, assuming Neumann boundary conditions (rigid walls, $\frac{\partial p}{\partial \mathbf{n}} = 0$), the solutions to the wave equation consist of linear combinations of its eigenfunctions [9]

$$\Phi_{nsm}(\rho, \theta, z) = J_n\left(\frac{\kappa_{ns}\rho}{b}\right)\cos\left(\frac{m\pi z}{h}\right)e^{in\theta}, \tag{2.10}$$

where n, s, and m are the circumferential, radial, and axial indices, respectively. n spans all integers while s and m span the positive integers (including 0). $J_n(\kappa_{ns}\rho/b)$ denotes the n'th order Bessel function of the first kind, where κ_{ns} is the s'th root of $J_n'(\kappa_{ns}) = 0$, so that the boundary condition at the walls of the cylinder ($\rho = b$) is fulfilled. $s = 0$ corresponds to the root of the Bessel derivative at the origin, which is only present when $n = 0$, since any higher order Bessel functions are all equal to 0 at the origin.

The value of the field within the cavity at any point, $\mathbf{r}$, due to an excitation at another point, $\mathbf{r}'$, can be described by the interior Neumann Green's function

$$G(\mathbf{r}|\mathbf{r}') = \sum_q \frac{\Phi_q(\mathbf{r})\Phi_q^*(\mathbf{r}')}{(k_q^2 - k^2)\int_V \Phi_q(\mathbf{r})\Phi_q^*(\mathbf{r})\mathrm{d}V}, \tag{2.11}$$

where q now represents all combinations of n, s, and m. Each eigenfunction Φ_q corresponds to an eigenfrequency, ω_q, given by

$$k_q = \sqrt{(\kappa_{ns}/b)^2 + (m\pi/h)^2} = \omega_q/c_0, \tag{2.12}$$

k is the wavenumber of the excitation, and V is the volume of the cavity. Given the the eigenfunctions from Equation 2.10 and the geometry described above, the integral in the denominator of Equation 2.11 can be evaluated as [10]

$$\begin{aligned}\int_V \Phi_q(\mathbf{r})\Phi_q^*(\mathbf{r})\mathrm{d}V &= \pi b^2\left(1 - n^2/\kappa_{ns}^2\right)J_n^2(\kappa_{ns})\frac{h}{\epsilon_m} \\ \epsilon_m &= \begin{cases} 1 & \text{if } m = 0 \\ 2 & \text{if } m \neq 0. \end{cases}\end{aligned} \tag{2.13}$$

The pressure at any point in the cavity is given by

$$p(\mathbf{r}) = p_0 G(\mathbf{r}|\mathbf{r}'), \tag{2.14}$$

where p_0 is a scaling factor that depends on the strength of the excitation. The total pressure field from multiple simultaneous excitations can be calculated as a sum over point sources weighted by their complex excitation amplitudes.

3 Method

3.1 Experimental setup

For the experimental setup a hard plastic cylinder of height of 95.35 mm and inner diameter of 56.30 mm was used. A metal disc with a hole of 1 cm in diameter was used as a ceiling. The cylinder was placed on a plane rectangular transducer array with 1 cm spacing between the centers of the transducers (Acoustophoretic Board by Interact Lab), as seen in Figure 3.1. Styrofoam beads of approximately 1 to 2 mm radii were manually placed in the cylinder through the hole in the top of the cylinder, by use of a netted placement rod (see for example Figure 4.15).

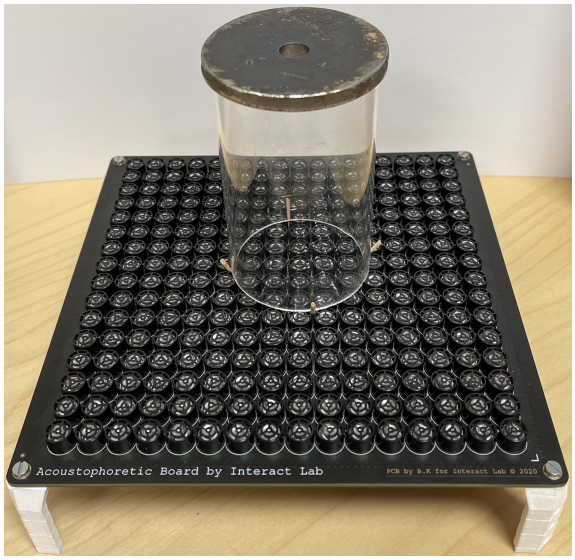

Figure 3.1: The experimental setup.

Two placements of the cylinder on the array were considered. One with the cylinder centered above a single transducer (see Figure 3.2a), and one centered in between four transducers (see Figure 3.2b). Because all transducers are positioned in the same plane, the excitation of axial modes will not differ between the the two setup options. The radial and circumferential components of the modes are coupled (as seen in Equation 2.10) in such a way that the radial position of a transducer entirely determines what type of modes (i.e. what combinations of mode indices n, s, and m) are excited the most. Prioritizing a wider range of different radial transducer positions therefore appears to be a good choice.

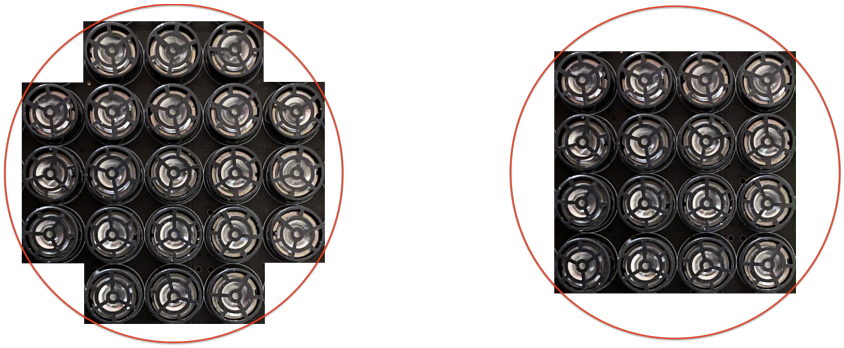

(a) Centering on a single transducer.

(b) Centering in between four transducers.

Figure 3.2: The two considered cylinder placements on the transducer array. The red circles show the cylinder wall boundary.

The four transducer centering option has transducers placed at three different distances from the center, while the single transducer centering has five. The single transducer centering also fits five more transducers within the cylinder, which adds more degrees of freedom when constructing sound fields. For these reasons the single transducer centering option was selected.

3.2 Calculation of the sound field

The total sound field in the cylinder is calculated as a superposition of the fields from each individual transducer, which in turn are calculated by summation of mode shapes in accordance with Equation 2.14. The transducers are assumed to be point sources.

The summation of modes is an infinite sum, that for practical applications must be truncated at some point. A method for the selection of what modes to include in the sound field calculation has been developed for this purpose. The selection is done by first compiling a list of modes and their modal amplitudes, calculated as $(k_q^2 - k^2)^{-1}$ (compare with Equation 2.11), for frequencies up to a point well above what is needed for an accurate representation of the sound field. The largest modal amplitude is then compared to all others, whereupon a selection of modes within a user specified dB range below the maximal modal amplitude is made. This final collection of modes is then used for the full calculation of the sound field. Note that this does not take into consideration how much a specific mode is excited with regards to transducer positions, nor what the amplitude at the considered trap position is. The main aim of this process is to reduce the time of the full calculation, so taking these things into account at this stage of the calculation would defeat the purpose. Instead, this method sorts through the modes with respect to their largest possible amplitudes throughout the cylinder, with the assumption that this generally corresponds to the maximum impact on the calculations.

For determining the forces and force gradients, the pressure field as well as all permutations of its first, second, and third order partial derivatives must be calculated,

as is made evident by Equation 2.1 in combination with Equations 2.7 and 2.8. This results in 19 mode shape derivatives in total, which are presented in Appendix A. These derivatives can be taken before the field summation, since the derivative is a linear operation. The force calculation is not linear with respect to the modal and transducer superpositions, however, and must be performed after the full summation is done. The derivatives are expressed and implemented in Cartesian coordinates, for ease of integration with already existing software.

The transducers used in the array operate at a frequency of 40 kHz, and are rated for a free field sound pressure of 6 Pa at a distance of 1 m, straight in front of a single transducer operating at maximum amplitude.[11] For free field calculations this corresponds to scaling the corresponding Green's function with $p_0 = 6\,\mathrm{N/m}$ (analogous to Equation 2.14), but it might not necessarily hold within the geometry of a cylinder. Two measurements were made of the sound pressure level within the cylinder. One with a single transducer at max amplitude, centered at the bottom of the cylinder, and one with all transducers at max amplitude (using the setup described in Section 3.1, with the cylinder centering seen in Figure 3.2b). The highest sound pressure level measured in the cylinder was 152.6 dB for the single transducer case, and 161 dB with all transducers active. The simulated sound pressure level, using $p_0 = 6\,\mathrm{N/m}$, has a maximum sound pressure level of 153.1 dB for the single transducer case, and 161.9 dB with all transducers active. The simulated and measured values are within 1 dB of each other, which was deemed close enough. Therefore, a p_0 of $6\,\mathrm{N/m}$ is used for all calculations.

3.3 Constructing acoustic traps

For the construction of acoustic traps an optimization problem with the objective function,

$$O(\mathbf{r}, A_1, ..., A_n) = w_F|\mathbf{F}(\mathbf{r}) + m\mathbf{G}|^2 + w_S\nabla\cdot\mathbf{F}(\mathbf{r}) + w_C\sum_{i,j}\Big|\frac{\partial F_{x_i}}{\partial x_j}(1-\delta_{i,j})\Big|^2, \quad (3.1)$$

is used, where $(x, y, z) = (x_1, x_2, x_3)$ and $\delta_{i,j}$ is the Kronecker delta. w_F, w_S, and w_C are the weight values applied to the force, stiffness, and cross term gradient parts of the objective function, respectively. This objective function is minimized at a chosen point $\mathbf{r}$ by numerical optimization (specifically the Broyden–Fletcher–Goldfarb–Shanno algorithm[12, 13]) with respect to the complex amplitudes A_1 through A_n, which contain the phase and amplitude for each of the n transducers in the setup.

The minimization process is performed in two steps. First one optimization where only the phases of the transducers are varied, and the starting point phases are set to random values. Then one additional optimization where both the phases and amplitudes are varied, using the resulting phases from the first optimization as a starting point. This avoids an occasional problem where the optimization process results in one or more of the transducers being turned off rather than shifted in phase when its initial starting point phase does not contribute nicely to the desired field. Note that if a phase cannot be found where a transducer contributes nicely, it will still be turned off at the second stage of the optimization.

Normalizing values of $w_F = \frac{1}{(mg)^2}$, $w_S = \frac{a}{mg}$, and $w_C = (\frac{a}{mg})^2$ seem to work well as a starting point when tuning the cost function weights. From here the weights are multiplied by values depending on what the resulting forces at and around the desired trap position look like. If the forces at the center of the trap is not equal to zero w_F needs to be increased, if the direct gradients of the force around the trap are not negative w_S needs to be increased, and if the cross term gradient is not zero w_C needs to be increased. For some positions, finding the perfect balance of weights might be harder than for others, and all three criteria might not be easily met all at once. Some compromising may therefore be required. Note that it is the relative size of the weights that matter, so weights of $w_F = 10$, $w_S = 5$, and $w_C = 1$ is equivalent to weights of $w_F = 20$, $w_S = 10$, and $w_C = 2$, for example.

3.4 Kinematic simulation

In order to verify (at least internally within the used model) that a certain pressure field does indeed produce a trap at the desired position, a kinematic simulation of a bead placed near the trap was made. This was done by setting up the equation of motion (Newton's second law) for a bead in the calculated sound field, with air resistance taken into account, and solving the resulting differential equation

$$m\ddot{\mathbf{r}} = m\mathbf{G} + \mathbf{F}_{\text{rad}} + \mathbf{F}_{\text{drag}}, \tag{3.2}$$

where

$$\mathbf{F}_{\text{drag}} = -\frac{\pi a^2 \rho_*}{2} C_D \dot{\mathbf{r}} \|\dot{\mathbf{r}}\| \tag{3.3}$$

is the force on the bead due to drag [14], $\mathbf{F}_{\text{rad}}$ is the acoustic radiation force from Equation 2.1, and $\mathbf{r}$ is the position of the bead (with dots indicating derivatives with respect to time). C_D is the drag force coefficient which relates to the Reynolds number R, empirically modelled by Brown-Lawler[15] as

$$C_D = \frac{24}{R}(1 + 0.15R^{0.681}) + \frac{0.407}{1 + \frac{8710}{R}}. \tag{3.4}$$

The Reynolds number is given by

$$R = \frac{2a}{\eta}\|\dot{\mathbf{r}}\|, \tag{3.5}$$

where η is the kinematic viscosity of the air. Equation 3.3 is solved numerically using a Runge-Kutta method (RK45), as implemented in the SciPy Python library[12], to obtain the travel path of a bead placed near the trap.

4 Results

This section presents simulations and experimental results, as well as a convergence study for the mode selection method described in Section 3.2. Three traps at different positions, dubbed trap position 1, 2, and 3, were simulated through tuning of the objective function weights of Equation 3.1 and calculation of the sound field using the resulting complex amplitudes.

Section 4.1 presents force diagrams for the three simulated cases, showing the acoustic radiation forces in nearby regions of the trap positions. Section 4.2 shows visualizations of the calculated sound field in the cylinder for each simulated case. Section 4.3 presents the kinematic simulation results, showing the path of beads placed near the three trap positions. The convergence study is presented in Section 4.4. Finally, experimental results from testing the experimental setup (see Section 3.1) using the complex amplitudes of one of the simulated traps, trap position 1, is presented in Section 4.5.

4.1 Force diagrams

This section presents force diagrams for three different trap positions, showing how the three force components F_x, F_y, and F_z change for displacements along the x, y, and z axes, using a 3 by 3 grid of graphs. The three graphs on the left show the x, y, and z components of the force (normalized by mg), for a displacement along the x axis from the trap position. The three graphs in the center and to the right do the same for displacements along the y and z axes, respectively. The Cartesian coordinate system for these diagrams is always oriented such that the x axis points in the radial direction. The gravitational force itself is not included in these diagrams, so a trap should have a force of $F_z/mg = 1$ at the trap position in order to cancel out the downwards force of gravity, while F_x and F_y should be equal to 0. The cost function weights used for the traps are presented as normalized values, where $w_F = \frac{1}{(mg)^2}\bar{w}_F$, $w_S = \frac{a}{mg}\bar{w}_S$, and $w_C = (\frac{a}{mg})^2\bar{w}_C$.

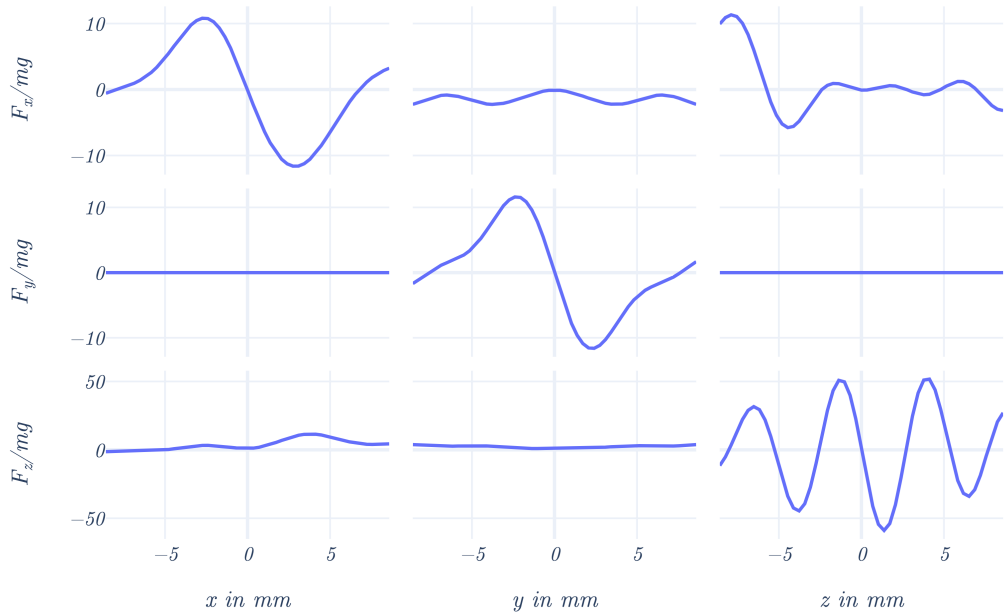

Figure 4.1: Force diagram for trap position 1, at $\rho = 15\,\text{mm}$, $\theta = 0$, and $z = h/2 = 47.675\,\text{mm}$.

Figure 4.1 shows the force diagram for a constructed trap at $\rho = 15\,\text{mm}$, $\theta = 0$, and $z = h/2 = 47.675\,\text{mm}$ (hereafter referred to as trap position 1), using the weights $\bar{w}_F = 15$, $\bar{w}_S = 1$, and $\bar{w}_C = 3$. The diagram shows negative direct gradients around the trap position with forces $F_x/mg \approx 874 \times 10^{-3}$, $F_y/mg \approx 193 \times 10^{-6}$, and $F_x/mg \approx 1.02$ at the trap position, which indicates that there should be a trap at the chosen position. In addition, the cross term curves are flat or close to flat, decreasing the risk for a bead placed in the trap to spiral away. Note, however, that the scale for F_z/mg is a lot larger than for F_x/mg and F_y/mg, going from -50 to 50. The bottom left graph might therefore seem flatter than it actually is at first glance, peaking at about 11.6 which is about the same size as the maximum of F_x/mg along the x axis. However, the important part is the flatness close to the trap position, since a small displacement along the x axis will still result in a stronger restoring force, F_x/mg. Even if the bead gets nudged in positive z direction by this cross term force, the much greater restoring force for displacements along the z axis (bottom right graph) should keep the bead trapped.

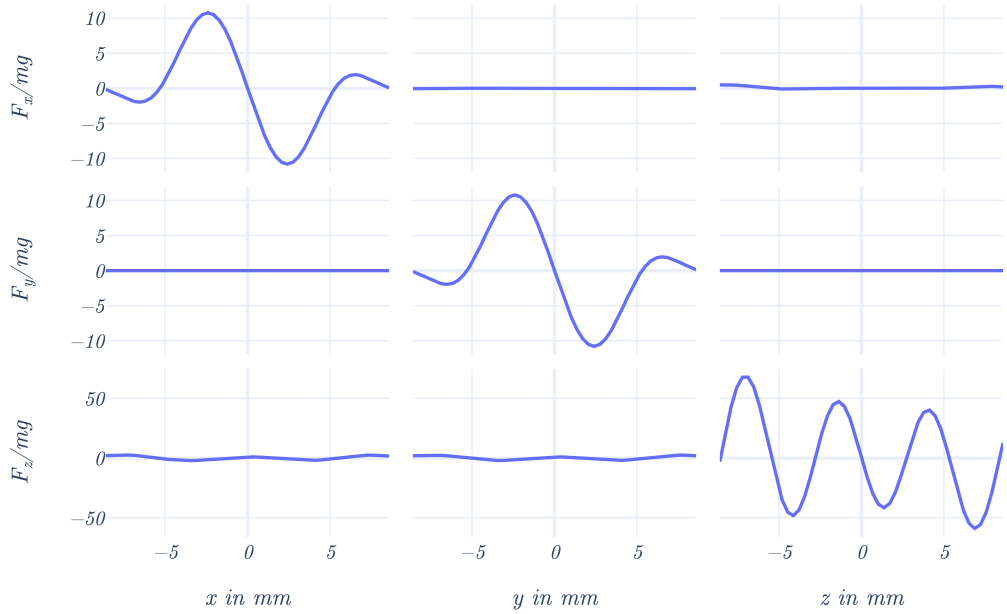

Figure 4.2: Force diagram for trap position 2, at $\rho = 0.01\,\text{mm}$, $\theta = 0$, and $z = h/2 = 47.675\,\text{mm}$ (trap position 2).

Figure 4.2 shows the force diagram for a trap placed at $\rho = 0.01\,\text{mm}$, $\theta = 0$, and $z = h/2 = 47.675\,\text{mm}$ (hereafter referred to as trap position 2), using the weights $\bar{w}_F = 1000$, $\bar{w}_S = 1$, and $\bar{w}_C = 0$. The trap was positioned slightly off center to avoid division by zero in the mode shape derivatives (see Appendix A). The diagram shows negative direct gradients around the trap position with forces $F_x/mg = 5.56 \times 10^{-6}$, $F_y/mg = 2.07 \times 10^{-9}$, and $F_z/mg = 0.997$. The cross terms for this trap are very flat, even without any cross term weighting applied. A lower weight for the force term would definitely be sufficient, but in this case it does not interfere with the negative gradients so a higher weight for even more precise positioning of the trap does not hurt.

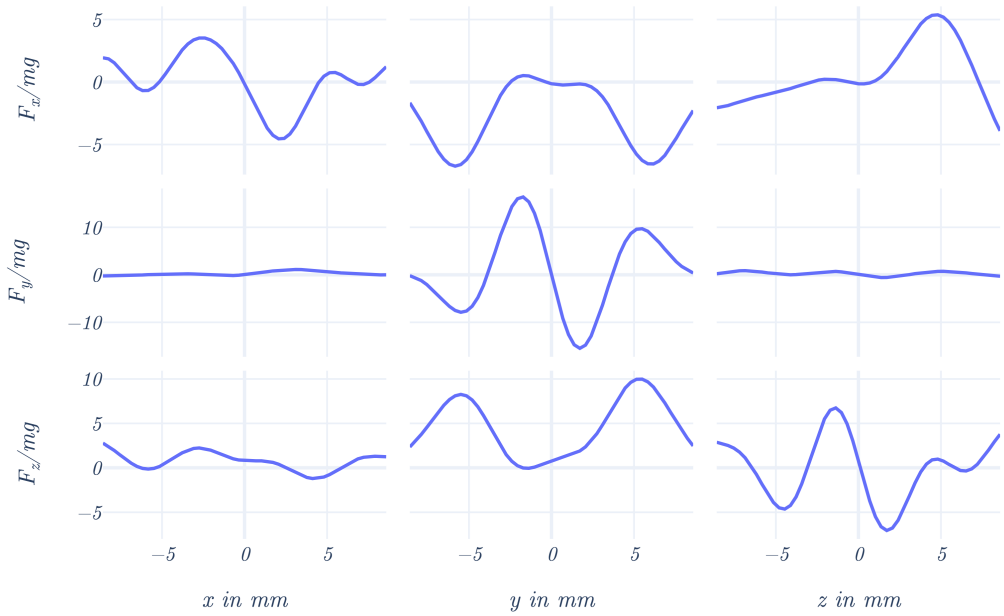

Figure 4.3: Force diagram for trap position 3, at $\rho = 10\,\text{mm}$, $\theta = \pi/4$, and $z = \frac{2}{3}h = 63.56\,\text{mm}$ (trap position 3).

Figure 4.3 shows the force diagram for a trap placed at $\rho = 10\,\text{mm}$, $\theta = \pi/4$, and $z = 2h/3 = 63.56\,\text{mm}$ (hereafter referred to as trap position 3), using the weights $\bar{w}_F = 8$, $\bar{w}_S = 3$, and $\bar{w}_C = 3$. The diagram shows negative direct gradients around the trap position with forces $F_x/mg = -0.137$, $F_y/mg = 4.57 \times 10^{-3}$, and $F_z/mg = 0.803$. This trap position required a bit more careful balancing of weights, since it was harder to fulfill all criteria for a trap at once. A compromise of settling for forces not quite equal to zero for F_x and not quite equal to one for F_z as well as not having very flat cross term gradients was made, in favour of ensuring negative direct gradients.

4.2 Field visualizations

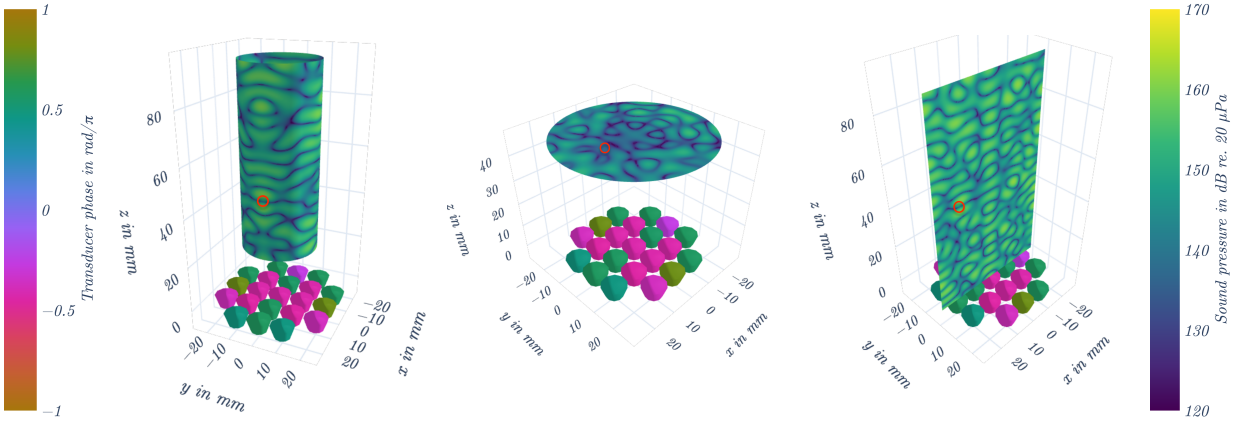

Figure 4.4: The sound field for trap 1, on a cylindrical surface of radius $\rho = 15\,\text{mm}$ to the left, in the xy plane at height $z = h/2$ in the middle, and in the xz plane to the right. The trap position is indicated by red circles.

Figure 4.4 shows the sound field for trap 1, evaluated on a cylindrical surface of radius $\rho = 15\,\text{mm}$ to the left, in the xy plane at height $z = h/2$ in the middle, and in the xz plane to the right. The trap position is indicated by red circles. There are higher sound pressure zones above and below the trap position, compared to the sound pressure surrounding the trap in the xy plane. This is in agreement with the higher stiffness along the z axis. The transducer phases form a symmetric pattern about the x axis, which results in a sound field symmetrical about the xz plane.

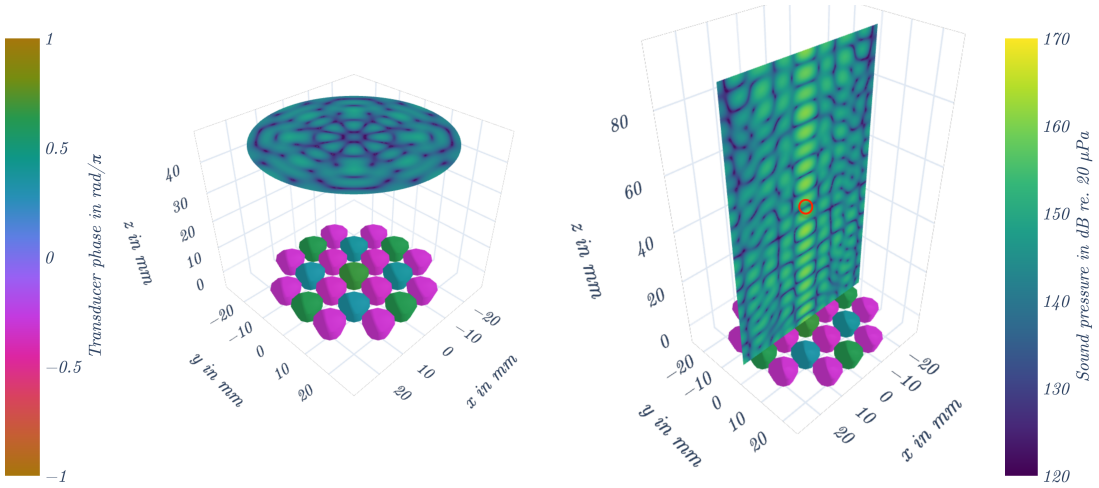

Figure 4.5: The sound field for trap 2, in the xy plane at height $z = h/2$ to the left, and in the xz plane to the right. The trap position is at the center of the left plot, and indicated by a red circle in the right plot.

Figure 4.5 shows the sound field for trap 2, evaluated in the xy plane at height

$z = h/2$ to the left, and in the xz plane to the right. The trap position is at the center of the left plot, and indicated by a red circle in the right plot. Again, there are higher sound pressure levels above and below the trap. The transducer phases as well as the sound field are symmetric under rotations of 90° about the z axis. This explains the near identical force curves along the x and y axes in Figure 4.2.

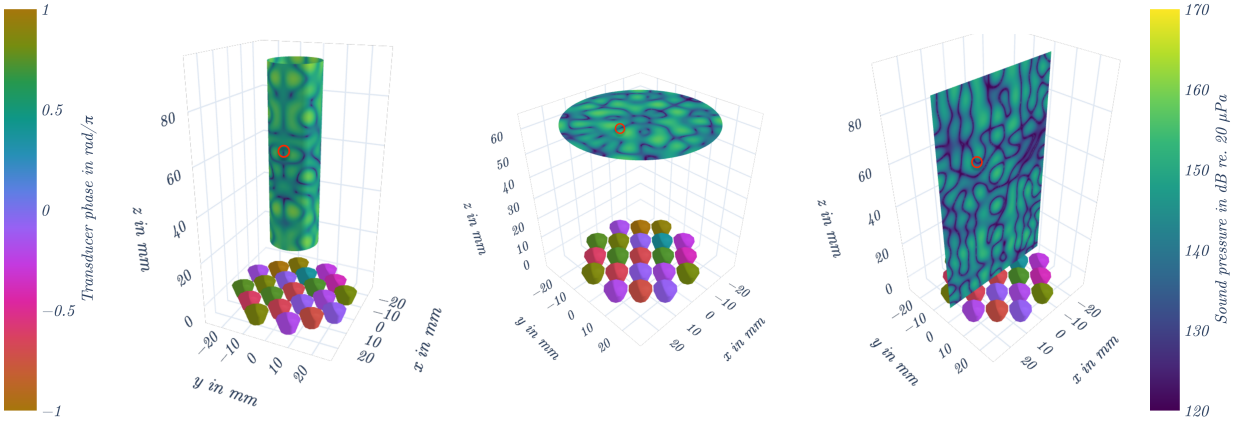

Figure 4.6: The sound field for trap 3, on a cylindrical surface of radius $\rho = 10\,\text{mm}$ to the left, in the xy plane at height $z = 2h/3$ in the middle, and in the xz plane to the right. The trap position is indicated by red circles.

Figure 4.6 shows the sound field for trap 3, evaluated on a cylindrical surface of radius $\rho = 10\,\text{mm}$ to the left, in the xy plane at a height of $z = 2h/3$ in the middle, and in the xz plane to the right. The trap position is indicated by red circles. The transducer phases show a kind of symmetric pattern about the x axis, with some transducers at mirrored positions having opposite phases (180° out of phase). For this trap the sound pressure is stronger on the sides of the trap on either side of the x axis, giving rise to the greater stiffness along the y axis. In x (radial) direction the field exhibits an almost (but not quite) nodal behaviour, which is why the stiffness along the x axis is lower.

4.3 Path simulation

This section presents the resulting paths from the kinematic simulations of beads placed near trap positions 1, 2, and 3. The starting position of the bead is 1 mm in positive x, y, and z direction away from the designated trap position in all three cases. The average position over time from 0.9 seconds to 1 second, where the bead oscillations are deemed to have died down sufficiently, is calculated as a measure of where the traps are actually located. These settling positions are indicated by the red lines in Figures 4.7 through 4.12. All plots are centered on their respective trap positions (so that the axes show displacements relative to the trap), with the x axis aligned with the radial direction.

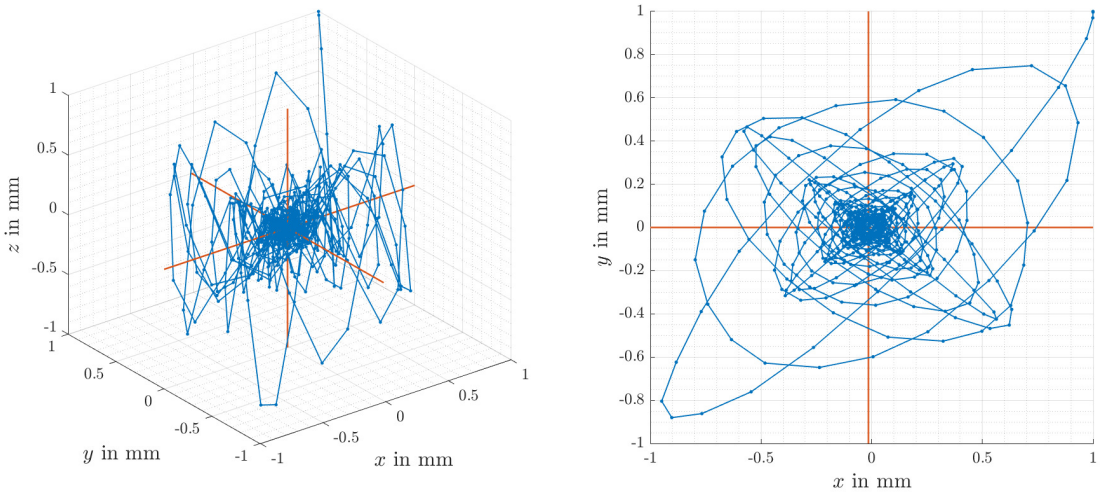

Figure 4.7: Path simulation result for a bead placed near trap position 1, shown as a 3D plot to the left, and in the xy plane to the right.

Figure 4.7 shows the simulated path of a bead placed near trap position 1 as a 3D plot to the left, and in the xy plane to the right. The bead spirals in towards the trap, closer and closer as it loses momentum due to the drag force. The average position of the final 0.1 seconds of the simulation, relative to the trap, is at $x = -14.6\,\mu\text{m}$, $y = 164\,\text{nm}$, and $z = 522\,\text{nm}$, very close to the designated position.

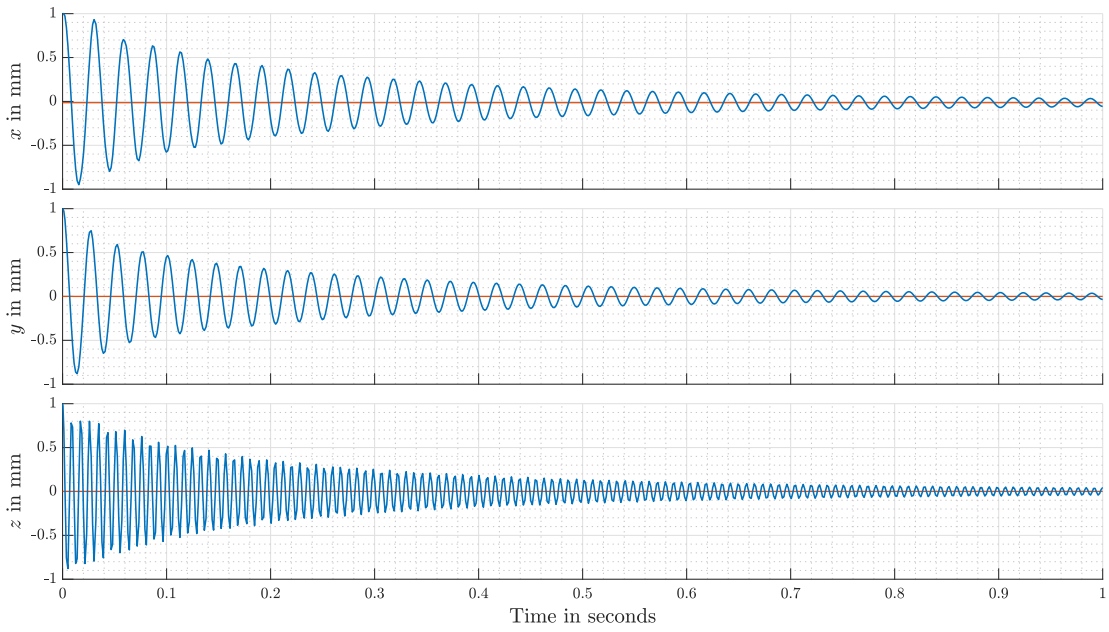

Figure 4.8: Path simulation result for a bead placed near trap position 1, shown in x, y, and z coordinates individually.

Figure 4.8 shows the bead position over time, split up individually as x, y, and z coordinates. This shows the damped oscillation of the bead along the three axes

more clearly. The frequencies of these oscillations can be related to the direct force gradients shown in Figure 4.1, where a steeper slope corresponds to a higher stiffness and therefore a higher oscillation frequency. The force gradient along the z axis is the largest one, so the oscillation in z direction has a higher frequency. The force gradients along the x and y axes are smaller (resulting in a lower frequency) and comparable in size to each other, which gives rise to the nice circling pattern seen in the xy plane plot of Figure 4.7.

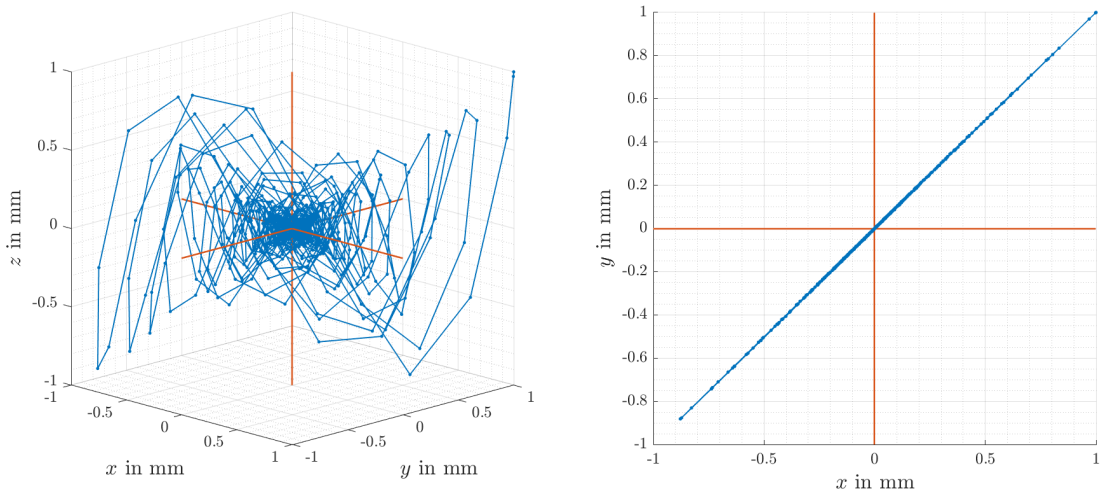

Figure 4.9: Path simulation result for a bead placed near trap position 2, shown as a 3D plot to the left, and in the xy plane to the right.

Figure 4.9 shows the simulated path of a bead placed near trap position 2 as a 3D plot to the left, and in the xy plane to the right. The oscillation around this trap also settles very close to the designated position, with average positions for the last 0.1 seconds of $x = 1.36\,\mu\text{m}$, $y = 1.39\,\mu\text{m}$, and $z = 0.891\,\mu\text{m}$.

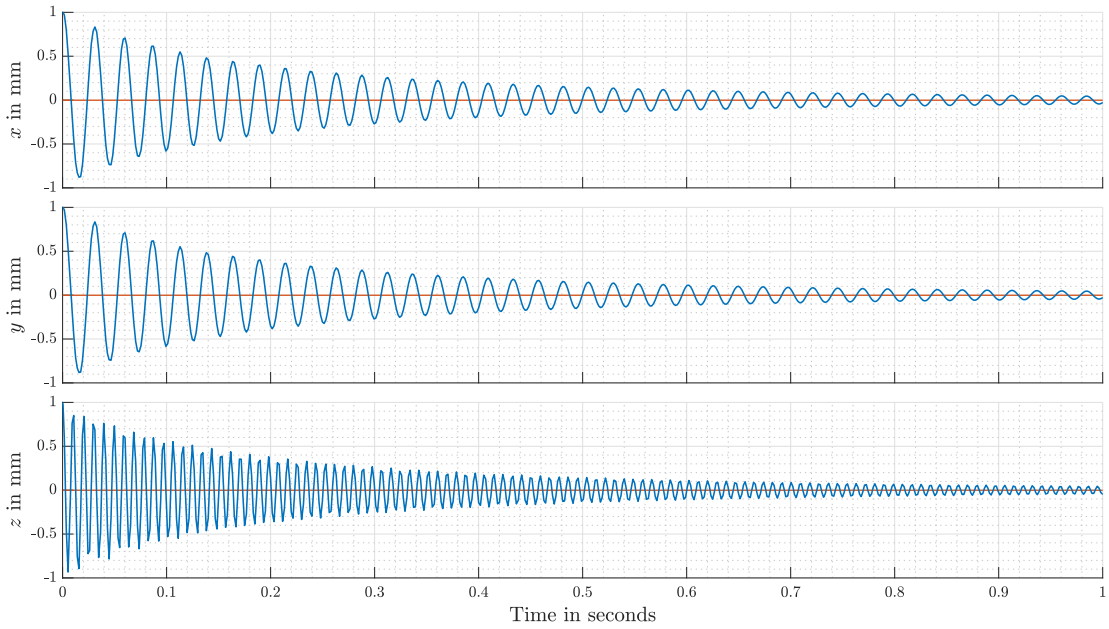

Figure 4.10: Path simulation result for a bead placed near trap position 2, shown in x, y, and z coordinates individually.

In the separated axis oscillations of Figure 4.10, it can be seen that the frequency of the oscillations along the z axis again is higher than for x and y, for the same reason as for trap 1. The x and y axis oscillations match almost perfectly which is also why the path traces out a straight line back and forth in the xy plot of Figure 4.9. This happens because the sound field is symmetric under 90° rotations about the z axis, as can be seen in Figure 4.5, which leads to symmetric forces along the x and y axes.

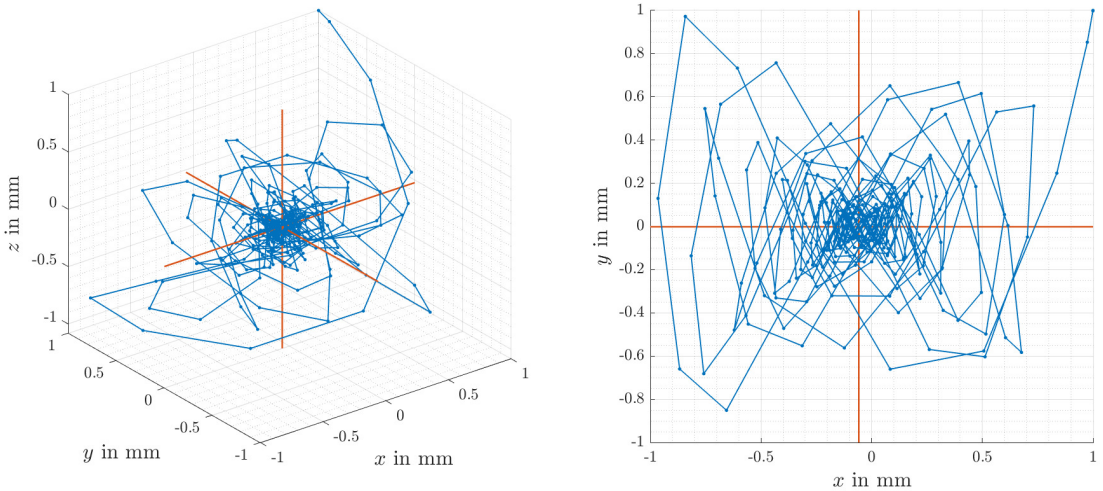

Figure 4.11: Path simulation result for a bead placed near trap position 3, shown as a 3D plot to the left, and in the xy plane to the right.

The simulated path of a bead placed near trap position 3 is shown in Figure 4.11,

as a 3D plot to the left, and in the xy plane to the right. The average positions for the last 0.1 seconds is $x = -58.2\,\mu\text{m}$, $y = -1.62\,\mu\text{m}$, and $z = -23.1\,\mu\text{m}$. Even with the compromise of the central forces being a bit further from the desired values (see Section 4.1), this is still well within any reasonable limits of accuracy.

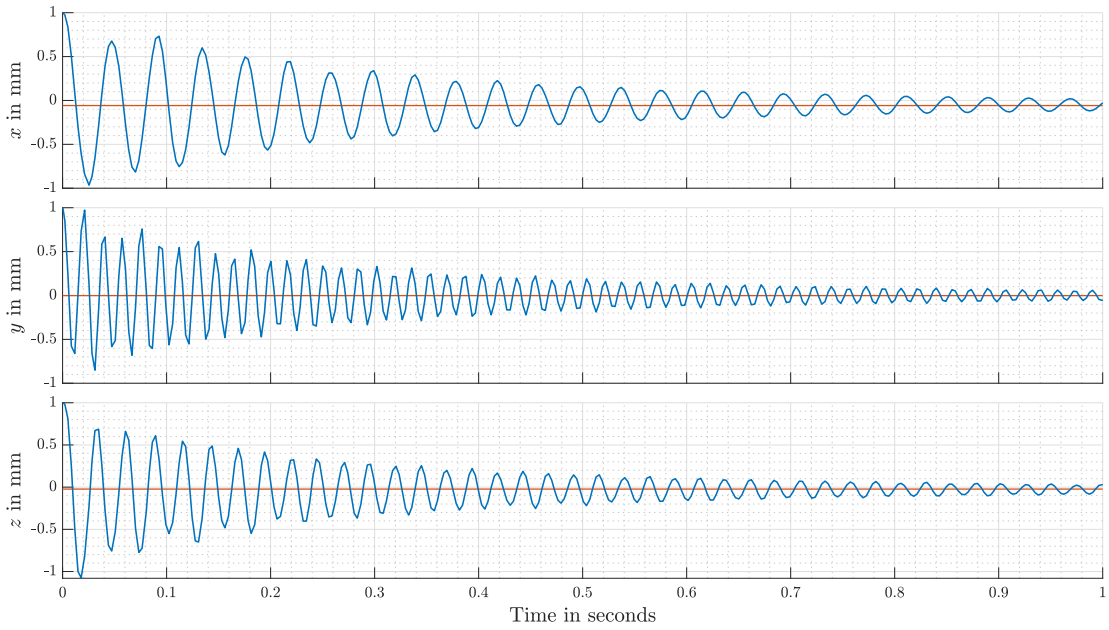

Figure 4.12: Path simulation result for a bead placed near trap position 3, shown in x, y, and z coordinates individually.

For trap 3 the oscillation along the y axis has the highest frequency, followed by z and then x, as can be seen in Figure 4.12, corresponding to the direct derivatives seen in Figure 4.3.

These simulations show that when driving the sound field using the complex amplitudes optimized for each case, there should be acoustic traps at the designated positions, provided that the model for calculating the sound field and radiation force agrees with reality.

4.4 Convergence study

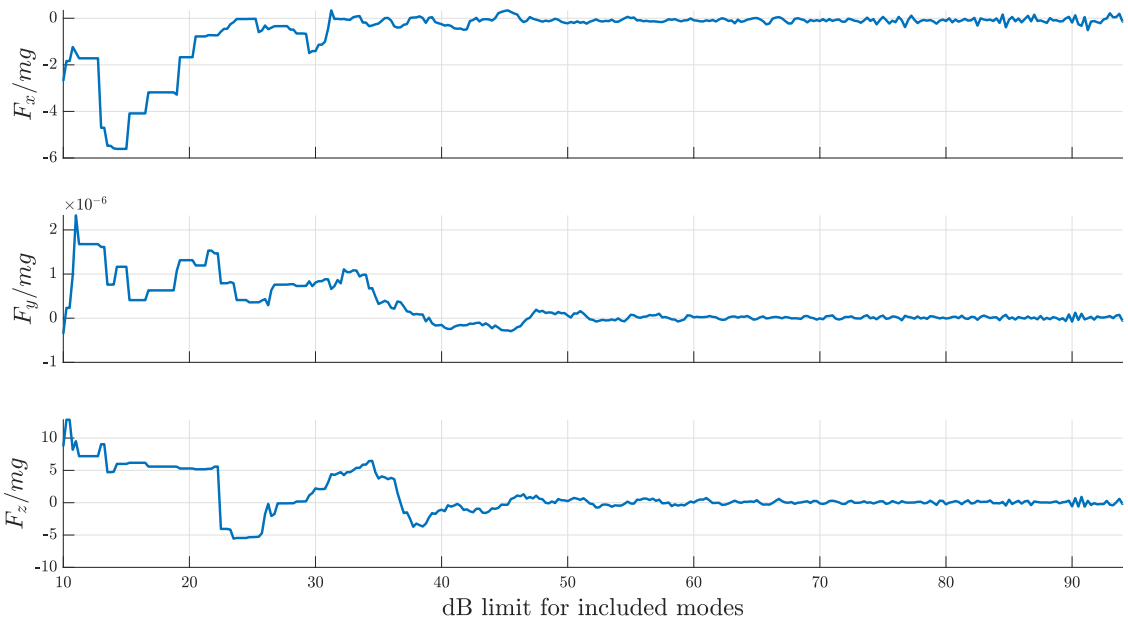

Figure 4.13: Forces in x, y, and z direction at the center of trap 1, plotted over different dB limits for the selection of modes.

Figure 4.13 shows the calculated force components at trap position 1 for different dB limits, where a higher dB limit includes more modes in the calculation, as described in Section 3.2. The gravitational force is included in the calculation, so F_z/mg should converge to zero, just like F_x/mg and F_y/mg. It can be seen that the forces have mostly converged by a limit of around 50 dB to 60 dB. At very high levels the errors seem to start fluctuating a bit more again. This could be because of numerical calculation errors due to the amplitudes of modes being added being very small. Corresponding plots for trap position 2 and 3 show similar behaviours and can be found in Appendix B.1.

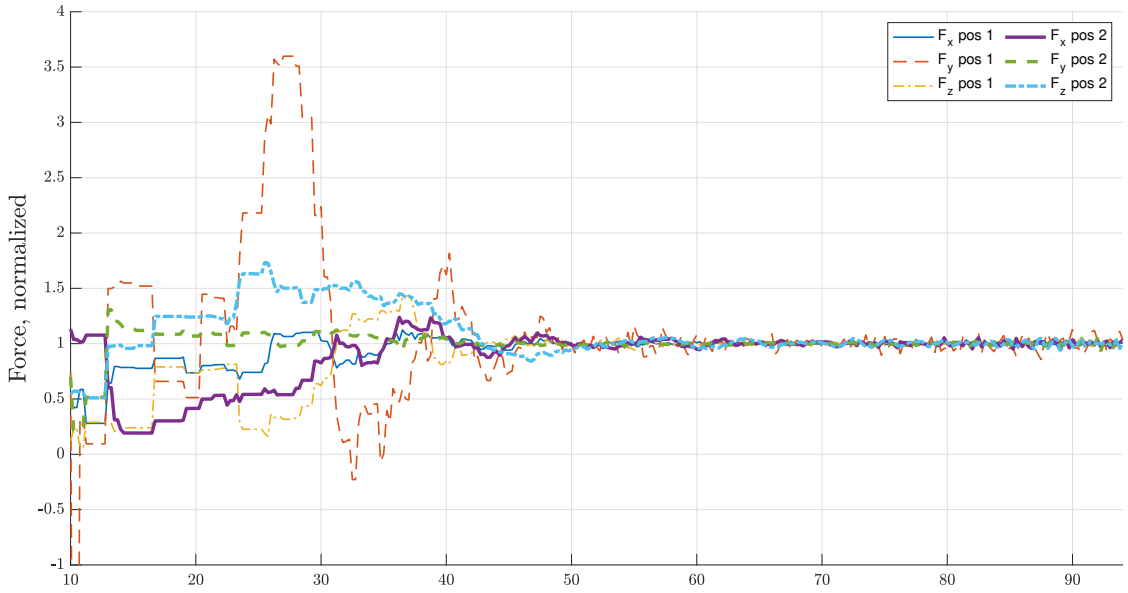

Figure 4.14: Forces in x, y, and z direction, at two different positions in a sound field driven by transducers of random phases, plotted over different dB limits for the selection of modes. The plotted forces are normalized by their average values above 60 dB.

Figure 4.14 shows the calculated force components at two different positions in a sound field driven by randomized transducer phases, for different dB limits. Position 1 is at $\rho = 7\,\text{mm}$, $\theta = \frac{5\pi}{16}$, $z = 74.7\,\text{mm}$, and position 2 is at $\rho = 12\,\text{mm}$, $\theta = \frac{\pi}{8}$, $z = 23.5\,\text{mm}$. The plotted forces are normalized by their average values between 60 dB and 94 dB (which is the highest dB limit considered). The forces can be seen to have mostly converged by about 60 dB to 70 dB, with fluctuations in error increasing slightly shortly thereafter.

A small inaccuracy of the forces at the center of a trap does not shift the trap position very much, as seen when comparing the settling positions of the path simulations in Section 4.3 to the designated trap positions. Traps with very weak direct gradients might be more sensitive though. There is also the matter of calculation time to consider, since the increase in number of modes included is approximately exponential for increasing dB limits. At a limit of 60 dB the number of modes included in the calculation is 4855, while 13996 are needed for 70 dB and 58376 are needed for 80 dB, which leads to greatly increased calculation times for higher dB limits. Because of these reasons a dB limit of 60 dB was deemed acceptable for the purposes of this thesis work.

4.5 Experimental test of trap 1

The trap at $\rho = 15\,\text{mm}$, $\theta = 0$, and $z = 47.675\,\text{mm}$ was tested experimentally with the setup described in Section 3.1. A trap at precisely the expected position was not found. Instead, three other traps, one approximately 1 cm above the expected one, one at the same height as the expected position but in the center of the cylinder, and one close to the center of the cylinder, but about 5 mm offset both radially and in height, was found. These alternate positions are referred to as trap 1a, 1b, and 1c, respectively. Pictures of beads trapped in the alternate positions are shown in Figures 4.15, 4.17, and 4.19.

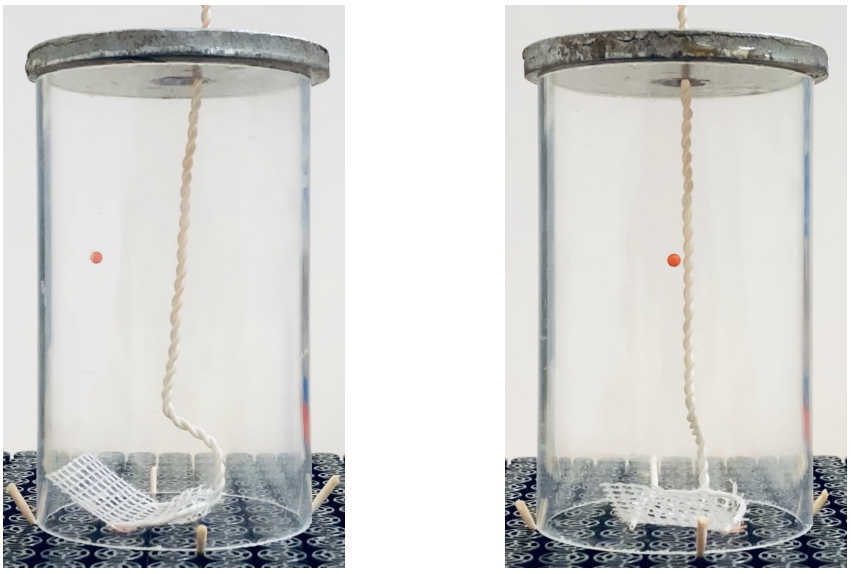

(a) x axis pointing to the left.

(b) x axis pointing towards the camera.

Figure 4.15: The first experimentally found trap, trap 1a, about 1 cm above the expected trap.

Figure 4.15 shows two pictures of a bead levitating in the first experimentally found trap. The bead is positioned at a height of $z \approx 3h/5 = 57.21\,\text{mm}$. It can be seen that the bead is about 15 mm off center along one of the array axes, since it is straight above the gap between the second and third outermost transducers to the left in the Figure 4.15a, and centered along the other as seen in Figure 4.15b. This is nearly 1 cm straight above trap position 1. This experimentally found trap is referred to as trap 1a, and has the approximate coordinates $\rho = 15\,\text{mm}$, $\theta = 0$, and $z = 57.21\,\text{mm}$.

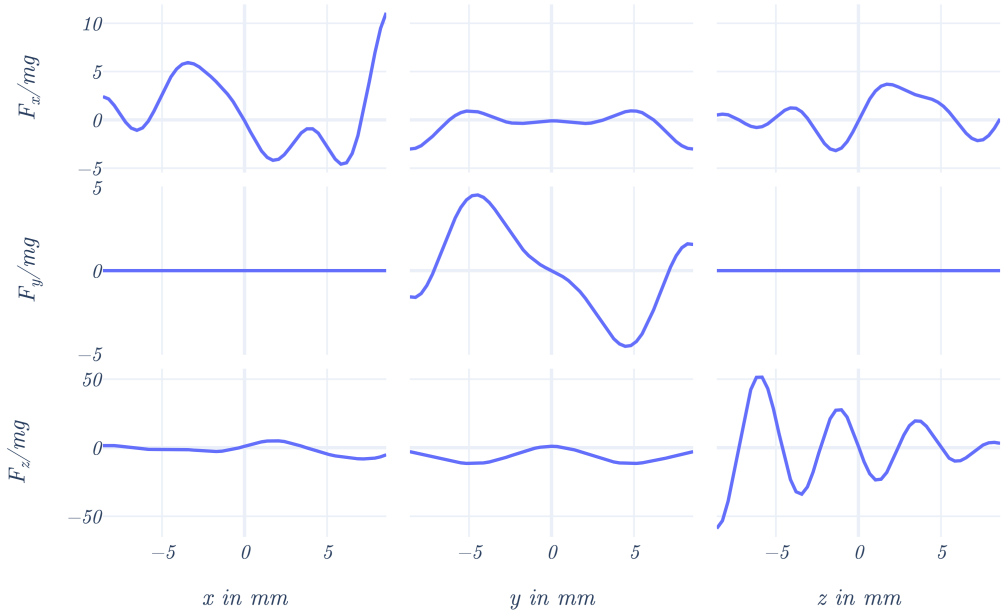

Figure 4.16: Force diagram for trap 1a, evaluated at $\rho = 15\,\text{mm}$, $\theta = 0$, and $z = 57.65\,\text{mm}$ in the field for trap 1.

Figure 4.16 shows the forces evaluated in the nearby region of trap 1a (Figure 4.15), centered at $\rho = 15\,\text{mm}$, $\theta = 0$, and $z = 57.65\,\text{mm}$. This is within a millimeter from the experimentally found trap and about one centimeter above the expected position, trap position 1. The direct gradients are negative around the trap position with forces $F_x/mg = -94.1 \times 10^{-3}$, $F_y/mg = 377 \times 10^{-3}$, and $F_z/mg = 1.03$. The cross term gradients are relatively flat, with the exception of the F_x force along the z axis and the F_z force along the x axis.

Figure 4.17: The second experimentally found trap, trap 1b, in the center of the cylinder both in radial and axial direction.

Figure 4.17 shows a picture of a bead levitating in the second experimentally found trap, trap 1b. It is centered in the cylinder both radially and axially.

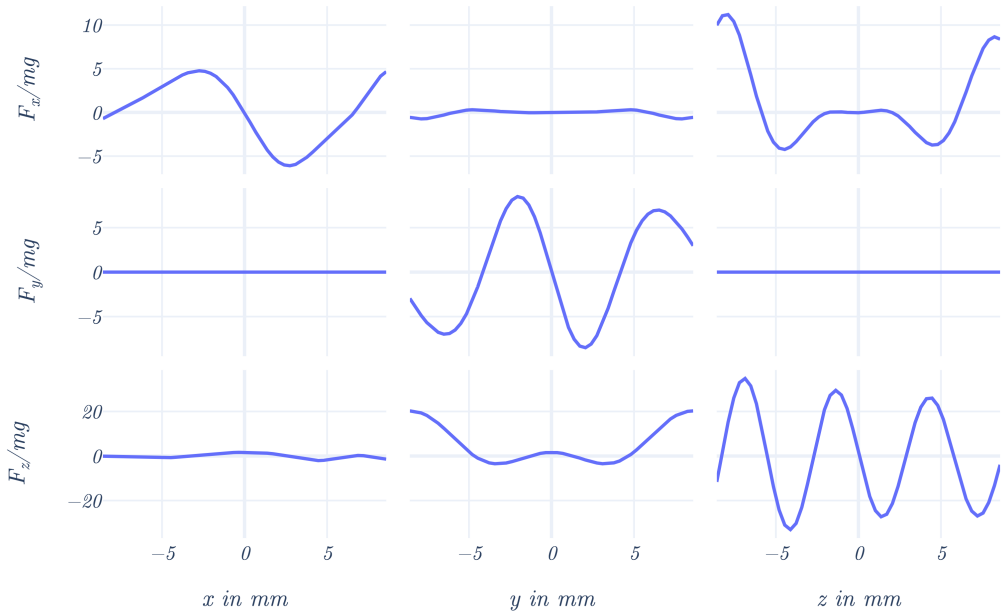

Figure 4.18: Force diagram for trap 1b, evaluated at $\rho = 0.65\,\text{mm}$, $\theta = \pi$, and $z = 47.275\,\text{mm}$ in the field for trap 1.

Figure 4.18 shows the forces evaluated in the nearby region of trap 1b (Figure 4.17), centered at $\rho = 0.65\,\text{mm}$, $\theta = \pi$, and $z = 47.275$ (0.4 cm below the center of the cylinder). This is again within a millimeter from the experimentally found trap. The direct gradients are negative around the trap position with forces $F_x/mg = -34.7 \times 10^{-3}$, $F_y/mg = 49.1 \times 10^{-6}$, and $F_z/mg = 1.66$. The cross term gradients are very flat.

These two first alternative traps were also verified with path simulations, analogous to those presented in Section 4.3, with settling points within a few hundredths of a millimeter from the central evaluation points of the force diagrams in Figure 4.16 and 4.18 (see Appendix B.2 for plots).

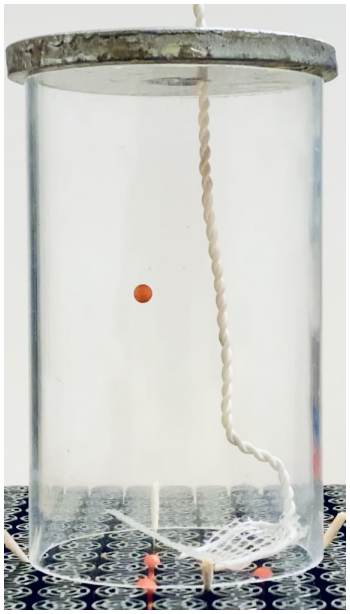

Figure 4.19: The third experimentally found trap, trap 1c, about 5 mm out radially from the center and about 5 mm above half the height off the cylinder.

Figure 4.19 shows a picture of a bead levitating in the third experimentally found trap, trap 1c. It is positioned at about $\rho = 5\,\text{mm}$, $\theta = 0$, and $z \approx 9h/16 \approx 53.6\,\text{mm}$. This is close to the second experimentally found trap, trap 1b, but still a bit too far away to comfortably say it is the same trap but shifted for some reason.

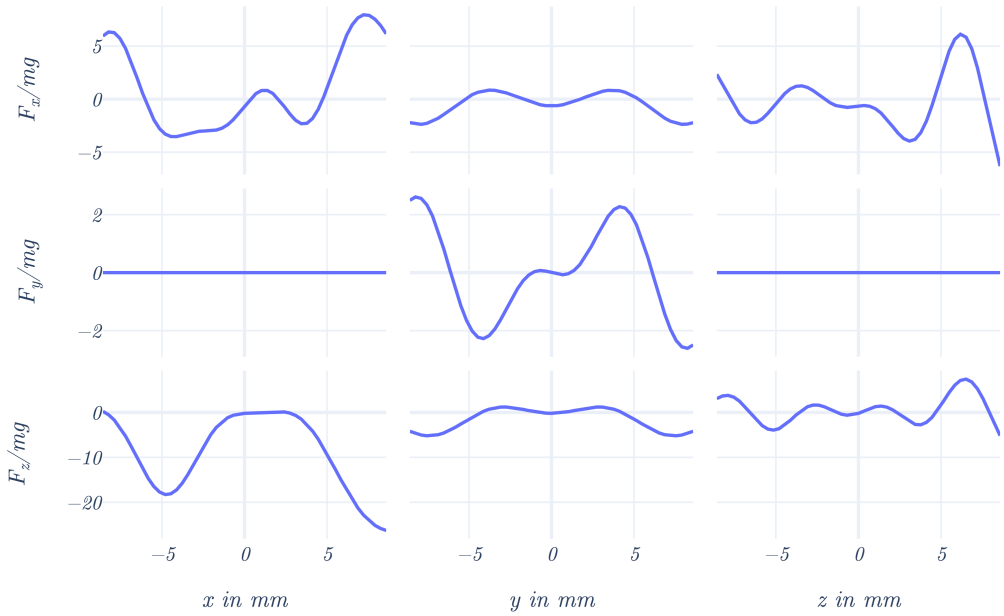

Figure 4.20: Force diagram for trap 1c, evaluated at $\rho = 5\,\text{mm}$, $\theta = 0$, and $z = 53.6\,\text{mm}$ in the field for trap 1.

Figure 4.20 shows the forces evaluated in the nearby region of trap 1c (Figure 4.19), centered at $\rho = 5\,\text{mm}$, $\theta = 0$, and $z = 53.6\,\text{mm}$. No negative direct gradients can be seen around this position, so the calculation model does not predict a trap position at this position.

5 Discussion

For the experimental test of trap position 1, no trap was found at the expected position. But the first two experimentally found traps, trap 1a and 1b, are located at positions where the model predicts traps, which suggests that the model might be valid, and that a trap at the expected position might also exist. The third found trap, trap 1c, which is not predicted by the model, suggests otherwise. There are some possible explanations for why the calculated sound field would not perfectly match the real case. The calculation method assumes point sources as transducers, which is not entirely accurate. Also, the bottom boundary of the cylinder is not a flat surface, as is assumed for the derivation of mode shapes, nor is the hole in the top boundary taken into account. Although the hole is quite small (1 cm in diameter), it is still larger in diameter than a wavelength at the excitation frequency ($\approx 8.58\,\text{mm}$), and could have an impact on the sound field. For these reasons the actual sound field could differ from calculations, although in what way and by how much is hard to say. Realistically these matters should also have an impact on the

first two experimentally found trap positions, so why it is only the third one that is not predicted correctly is not yet understood.

A natural next step for this calculation method would be to include the directive properties of the transducers. For the experimental application, a flat rigid boundary at the bottom of the cylinder could be more closely approximated in the future by filling the space in between the transducers so that it behaves more like a flat surface. The hole in the top of the cylinder is harder to do something about without an alternate way of placing beads in the sound field.

Placing beads in traps by hand is quite a fiddly task. The placement rod, like the bead itself, is also a sound scatterer and so it will disturb the trap when close. For the setup used the only access point was through the small hole in the top of the cylinder, which makes approaching the trap with the placement rod from the side, getting the shaft further away from the bead, impossible. It is also impossible with the current setup to remove the placement rod from the cylinder after a trap has been found.

There is also the problem that the constructed trap might not be the only trap within the cylinder (this seems to hold true in general, although more research is needed), and the bead might end up in one of these alternative traps instead. This seems to be what was observed with the alternate trap positions found at other positions than the designated trap position. There is also the risk of this being a coincidence, although it does seem a bit unlikely. With such complicated fields it is hard to say for sure, however.

An interesting area of future study would be to gather a more in depth mapping of where traps within a cylindrical geometry are easier or harder to construct, and perhaps even to find a general relationship between position and cost function weights needed for a trap. It would also be interesting to investigate different transducer array positioning patterns. As mentioned in Section 3.1, the types of modes excited is entirely determined by the radial position of transducers (for plane transducer arrays with all transducers at the same height), due to the coupling of radial and circumferential modes. The circumferential transducer position only determines the mode shape orientation, through rotation about the z axis, where one extremum of each circumferential mode shape component from any specific transducer always lies at the angle of that transducer. The orientation can also be controlled to some extent through differences in signal amplitude between transducer pairs placed at the same radial distance from the center but at different (non 180°) angles. This is true because the circumferential components of the mode shapes are described by harmonic functions, and the sum of harmonic functions of different phases and amplitudes result in a new harmonic function. Transducer configurations that maximize the number off different radial transducer positions, while having at least two transducers at each radial position but different circumferential positions, for controlling the orientation of the field, should excite more diverse collections of modes and might make traps at some positions easier to construct.

6 Conclusion

A method for calculating the sound field within a cylindrical cavity, and numerically optimizing transducer phases to construct acoustic traps has been developed. It has been shown that, at least internally within the model, the modes of a cylinder can be excited in such a way as to form acoustic traps at designated positions.

The possibility of levitation within a cylindrical cavity has also been shown experimentally. Even though no trap was experimentally found at a designated trap position, the fact that two of the traps found are also predicted by the model suggests that the model might be somewhat valid. A third experimentally found trap, which is not predicted by the model, suggests the opposite. More data needs to be collected before making any definitive conclusions, especially since only one of the simulated trap fields was tested experimentally.

References

[1] L. V. King, "On the acoustic radiation pressure on spheres," *Proceedings of the Royal Society of London. Series A - Mathematical and Physical Sciences*, vol. 147, no. 861, pp. 212–240, 1934. [Online]. Available: https://royalsocietypublishing.org/doi/abs/10.1098/rspa.1934.0215

[2] L. P. Gor'kov, "On the Forces Acting on a Small Particle in an Acoustical Field in an Ideal Fluid," *Soviet Physics Doklady*, vol. 6, p. 773, Mar. 1962.

[3] O. A. Sapozhnikov and M. R. Bailey, "Radiation force of an arbitrary acoustic beam on an elastic sphere in a fluid," *The Journal of the Acoustical Society of America*, vol. 133, no. 2, pp. 661–676, 2013. [Online]. Available: https://doi.org/10.1121/1.4773924

[4] T. Hoshi, Y. Ochiai, and J. Rekimoto, "Three-dimensional noncontact manipulation by opposite ultrasonic phased arrays," *Japanese Journal of Applied Physics*, vol. 53, no. 7S, p. 07KE07, jun 2014. [Online]. Available: https://doi.org/10.7567/jjap.53.07ke07

[5] A. Marzo, S. Seah, B. Drinkwater, D. Sahoo, B. Long, and S. Subramanian, "Holographic acoustic elements for manipulation of levitated objects," *Nature communications*, vol. 6, p. 8661, 10 2015.

[6] C. Andersson and J. Ahrens, "Reducing spiraling in transducer array based acoustic levitation," in *2020 IEEE International Ultrasonics Symposium (IUS)*, 2020, pp. 1–4.

[7] M. Barmatz and P. Collas, "Acoustic radiation potential on a sphere in plane, cylindrical, and spherical standing wave fields," *The Journal of the Acoustical Society of America*, vol. 77, no. 3, pp. 928–945, 1985. [Online]. Available: https://doi.org/10.1121/1.392061

[8] D. Xu, F. Cai, M. Chen, F. Li, C. Wang, L. Meng, D. Xu, W. Wang, J. Wu, and H. Zheng, "Acoustic manipulation of particles in a cylindrical cavity: Theoretical and experimental study on the effects of boundary conditions," *Ultrasonics*, vol. 93, p. 18—25, March 2019. [Online]. Available: https://doi.org/10.1016/j.ultras.2018.10.003

[9] E. G. Williams, *Fourier Acoustics: Sound Radiation and Nearfield Acoustical Holography*. Elsevier, 1999.

[10] E. Williams, "On green's functions for a cylindrical cavity," *Journal of The Acoustical Society of America - J ACOUST SOC AMER*, vol. 102, 12 1997.

[11] *MA40S4S/MA40S4R Ultrasonic Sensor Open Structure Type*, Murata Manufacturing Co., Ltd., 2020. [Online]. Available: https://www.murata.com/~/media/webrenewal/products/sensor/ultrasonic/open/datasheet_maopn.ashx?la=en

[12] P. Virtanen, R. Gommers, T. E. Oliphant, M. Haberland, T. Reddy, D. Cournapeau, E. Burovski, P. Peterson, W. Weckesser, J. Bright, S. van der Walt, M. Brett, J. Wilson, K. J. Millman, N. Mayorov, A. R. J. Nelson, E. Jones, R. Kern, E. Larson, C. J. Carey, I. Polat, Y. Feng, E. W. Moore, J. VanderPlas, D. Laxalde, J. Perktold, R. Cimrman, I. Henriksen, E. A. Quintero, C. R. Harris, A. M. Archibald, A. H. Ribeiro, F. Pedregosa, P. van Mulbregt, and SciPy, "Scipy 1.0-fundamental algorithms for scientific computing in python," *CoRR*, vol. abs/1907.10121, 2019. [Online]. Available: http://arxiv.org/abs/1907.10121

[13] C. Zhu, R. H. Byrd, P. Lu, and J. Nocedal, "Algorithm 778: L-bfgs-b: Fortran subroutines for large-scale bound-constrained optimization," *ACM Trans. Math. Softw.*, vol. 23, no. 4, p. 550–560, Dec. 1997. [Online]. Available: https://doi.org/10.1145/279232.279236

[14] F. M. White, *Fluid Mechanics. 8th ed.* McGraw-Hill Education, 2016.

[15] P. P. Brown and D. F. Lawler, "Sphere drag and settling velocity revisited," *Journal of Environmental Engineering*, vol. 129, no. 3, pp. 222–231, 2003. [Online]. Available: https://doi.org/10.1061/(ASCE)0733-9372(2003)129:3(222)

A Mode shape derivatives

The first, second, and third order partial derivatives of the mode shapes

$$\Phi_{nsm}(\rho,\theta,z) = J_n\left(\frac{\kappa_{ns}\rho}{b}\right)\cos\left(\frac{m\pi z}{h}\right)e^{in\theta}, \tag{A.1}$$

are presented below.

A.1 First order partial derivatives

$$\frac{\partial\Phi}{\partial x} = \frac{\kappa_{ns}\rho x J_{n-1}\left(\frac{\kappa_{ns}\rho}{b}\right) - bn(x+iy)J_n\left(\frac{\kappa_{ns}\rho}{b}\right)}{b\rho^2}\cos\left(\frac{\pi m z}{h}\right)e^{i\theta n} \tag{A.2}$$

$$\frac{\partial\Phi}{\partial y} = \frac{\kappa_{ns}\rho y J_{n-1}\left(\frac{\kappa_{ns}\rho}{b}\right) + ibn(x+iy)J_n\left(\frac{\kappa_{ns}\rho}{b}\right)}{b\rho^2}\cos\left(\frac{\pi m z}{h}\right)e^{i\theta n} \tag{A.3}$$

$$\frac{\partial\Phi}{\partial z} = -J_n\left(\frac{\kappa_{ns}\rho}{b}\right)\frac{\pi m}{h}\sin\left(\frac{\pi m z}{h}\right)e^{i\theta n} \tag{A.4}$$

A.2 Second order partial derivatives

$$\begin{aligned}\frac{\partial^2\Phi}{\partial x^2} = \frac{1}{b^2\rho^4}\Bigg\{ &\left(-\rho^2\left(b^2n+\kappa_{ns}^2x^2\right)+b^2n(x+iy)((n+2)x+iny)\right)J_n\left(\frac{\kappa_{ns}\rho}{b}\right)\\ &+b\kappa_{ns}\rho\left(\rho^2-2x(x+iny)\right)J_{n-1}\left(\frac{\kappa_{ns}\rho}{b}\right)\Bigg\}\cos\left(\frac{\pi m z}{h}\right)e^{i\theta n}\end{aligned} \tag{A.5}$$

$$\begin{aligned}\frac{\partial^2\Phi}{\partial y^2} = \frac{1}{b^2\rho^4}\Bigg\{ &b\kappa_{ns}\rho\left(2inxy+\rho^2-2y^2\right)J_{n-1}\left(\frac{\kappa_{ns}\rho}{b}\right)\\ &-\left(\kappa_{ns}^2\rho^2y^2+b^2n\left(\rho^2+(x+iy)(nx+i(n+2)y)\right)\right)J_n\left(\frac{\kappa_{ns}\rho}{b}\right)\Bigg\}\cos\left(\frac{\pi m z}{h}\right)e^{i\theta n}\end{aligned} \tag{A.6}$$

$$\frac{\partial^2\Phi}{\partial z^2} = -J_n\left(\frac{\kappa_{ns}\rho}{b}\right)\frac{\pi^2m^2}{h^2}\cos\left(\frac{\pi m z}{h}\right)e^{i\theta n} \tag{A.7}$$

$$\begin{aligned}\frac{\partial^2\Phi}{\partial x\partial y} = \frac{1}{b^2\rho^4}\Bigg\{ &ib\kappa_{ns}\rho(n(x-y)(x+y)+2ixy)J_{n-1}\left(\frac{\kappa_{ns}\rho}{b}\right)\\ &-i\left(b^2n\left(\rho^2+(x+iy)(nx+i(n+2)y)\right)-i\kappa_{ns}^2\rho^2xy\right)J_n\left(\frac{\kappa_{ns}\rho}{b}\right)\Bigg\}\cos\left(\frac{\pi m z}{h}\right)e^{i\theta n}\end{aligned} \tag{A.8}$$

$$\frac{\partial^2\Phi}{\partial x\partial z} = \frac{bn(x+iy)J_n\left(\frac{\kappa_{ns}\rho}{b}\right) - \kappa_{ns}\rho x J_{n-1}\left(\frac{\kappa_{ns}\rho}{b}\right)}{b\rho^2}\frac{\pi m}{h}\sin\left(\frac{\pi m z}{h}\right)e^{i\theta n} \tag{A.9}$$

$$\frac{\partial^2\Phi}{\partial y\partial z} = \frac{bn(y-ix)J_n\left(\frac{\kappa_{ns}\rho}{b}\right) - \kappa_{ns}\rho y J_{n-1}\left(\frac{\kappa_{ns}\rho}{b}\right)}{b\rho^2}\frac{\pi m}{h}\sin\left(\frac{\pi m z}{h}\right)e^{i\theta n} \tag{A.10}$$

A.3 Third order partial derivatives

$$\frac{\partial^3\Phi}{\partial x^3} = \frac{1}{b^3\rho^6}\Bigg\{\kappa_{ns}\rho\left(b^2x\left(\left(n^2+8\right)x^2-3n^2y^2+12inxy\right)-\rho^2\left(\kappa_{ns}^2x^3+b^2(6x+3iny)\right)\right)J_{n-1}\left(\frac{\kappa_{ns}\rho}{b}\right) \\ +b\left(b^2n\left(\rho^2(3(n+2)x+i(3n+2)y)-(x+iy)((n+2)x+iny)((n+4)x+iny)\right)+\kappa_{ns}^2\rho^2x\left(-3\rho^2+x((n+4)x+3iny)\right)\right)J_n\left(\frac{\kappa_{ns}\rho}{b}\right)\Bigg\}\cos\left(\frac{\pi mz}{h}\right)e^{i\theta n} \tag{A.11}$$

$$\frac{\partial^3\Phi}{\partial y^3} = \frac{1}{b^3\rho^6}\Bigg\{\kappa_{ns}\rho\left(b^2y\left(-3n^2x^2+\left(n^2+8\right)y^2-12inxy\right)-\rho^2\left(\kappa_{ns}^2y^3+b^2(6y-3inx)\right)\right)J_{n-1}\left(\frac{\kappa_{ns}\rho}{b}\right) \\ +b\left(b^2n\left(\rho^2(3(n+2)y-i(3n+2)x)+(x+iy)(nx+i(n+2)y)((n+4)y-inx)\right)+\kappa_{ns}^2\rho^2y\left(-3\rho^2+y((n+4)y-3inx)\right)\right)J_n\left(\frac{\kappa_{ns}\rho}{b}\right)\Bigg\}\cos\left(\frac{\pi mz}{h}\right)e^{i\theta n} \tag{A.12}$$

$$\frac{\partial^3\Phi}{\partial z^3} = J_n\left(\frac{\kappa_{ns}\rho}{b}\right)\frac{\pi^3m^3}{h^3}\sin\left(\frac{\pi mz}{h}\right)e^{i\theta n} \tag{A.13}$$

$$\frac{\partial^3\Phi}{\partial x^2\partial y} = \frac{1}{b^3\rho^6}\Bigg\{b\left(b^2n\left(\rho^2(-(n-2)y+i(n+2)x)+i(x+iy)((n+2)x+iny)(nx+i(n+4)y)\right)+\kappa_{ns}^2\rho^2\left(-\rho^2y+x\left(-inx^2+(n+4)xy+2iny^2\right)\right)\right)J_n\left(\frac{\kappa_{ns}\rho}{b}\right) \\ -\kappa_{ns}\rho\left(\kappa_{ns}^2\rho^2x^2y+b^2\left(n^2\left(y^3-3x^2y\right)+inx\left(\rho^2+2x^2-10y^2\right)+2y\left(\rho^2-4x^2\right)\right)\right)J_{n-1}\left(\frac{\kappa_{ns}\rho}{b}\right)\Bigg\}\cos\left(\frac{\pi mz}{h}\right)e^{i\theta n} \tag{A.14}$$

$$\frac{\partial^3\Phi}{\partial x^2\partial z} = \frac{\left(\kappa_{ns}^2\rho^2x^2+b^2n\left(\rho^2-(x+iy)((n+2)x+iny)\right)\right)J_n\left(\frac{\kappa_{ns}\rho}{b}\right)+b\kappa_{ns}\rho\left(-\rho^2+2x(x+iny)\right)J_{n-1}\left(\frac{\kappa_{ns}\rho}{b}\right)}{b^2\rho^4}\frac{\pi m}{h}\sin\left(\frac{\pi mz}{h}\right)e^{i\theta n} \tag{A.15}$$

$$\frac{\partial^3\Phi}{\partial y^2\partial x} = \frac{1}{b^3\rho^6}\Bigg\{b\left(b^2n\left((x+iy)((n+4)x+iny)(nx+i(n+2)y)-\rho^2((n-2)x+i(n+2)y)\right)+\kappa_{ns}^2\rho^2\left(-\rho^2x+y\left(-2inx^2+(n+4)xy+iny^2\right)\right)\right)J_n\left(\frac{\kappa_{ns}\rho}{b}\right) \\ -\kappa_{ns}\rho\left(\kappa_{ns}^2\rho^2xy^2+b^2\left(n^2\left(x^3-3xy^2\right)-iny\left(\rho^2-10x^2+2y^2\right)+2x\left(\rho^2-4y^2\right)\right)\right)J_{n-1}\left(\frac{\kappa_{ns}\rho}{b}\right)\Bigg\}\cos\left(\frac{\pi mz}{h}\right)e^{i\theta n} \tag{A.16}$$

$$\frac{\partial^3\Phi}{\partial y^2\partial z} = \frac{\left(\kappa_{ns}^2\rho^2y^2+b^2n\left(\rho^2+(x+iy)(nx+i(n+2)y)\right)\right)J_n\left(\frac{\kappa_{ns}\rho}{b}\right)-b\kappa_{ns}\rho\left(2inxy+\rho^2-2y^2\right)J_{n-1}\left(\frac{\kappa_{ns}\rho}{b}\right)}{b^2\rho^4}\frac{\pi m}{h}\sin\left(\frac{\pi mz}{h}\right)e^{i\theta n} \tag{A.17}$$

$$\frac{\partial^3\Phi}{\partial z^2\partial x} = \frac{-\kappa_{ns}\rho xJ_{n-1}\left(\frac{\kappa_{ns}\rho}{b}\right)+bn(x+iy)J_n\left(\frac{\kappa_{ns}\rho}{b}\right)}{b\rho^2}\frac{\pi^2m^2}{h^2}\cos\left(\frac{\pi mz}{h}\right)e^{i\theta n} \tag{A.18}$$

$$\frac{\partial^3\Phi}{\partial z^2\partial y} = \frac{-\kappa_{ns}\rho yJ_{n-1}\left(\frac{\kappa_{ns}\rho}{b}\right)+bn(y-ix)J_n\left(\frac{\kappa_{ns}\rho}{b}\right)}{b\rho^2}\frac{\pi^2m^2}{h^2}\cos\left(\frac{\pi mz}{h}\right)e^{i\theta n} \tag{A.19}$$

$$\frac{\partial^3\Phi}{\partial x\partial y\partial z} = \frac{\left(\kappa_{ns}^2\rho^2xy+ib^2n\left(\rho^2+(x+iy)(nx+i(n+2)y)\right)\right)J_n\left(\frac{\kappa_{ns}\rho}{b}\right)+b\kappa_{ns}\rho(2xy-in(x-y)(x+y))J_{n-1}\left(\frac{\kappa_{ns}\rho}{b}\right)}{b^2\rho^4}\frac{\pi m}{h}\sin\left(\frac{\pi mz}{h}\right)e^{i\theta n} \tag{A.20}$$

B Additional plots

B.1 Convergence for trap 2 and 3

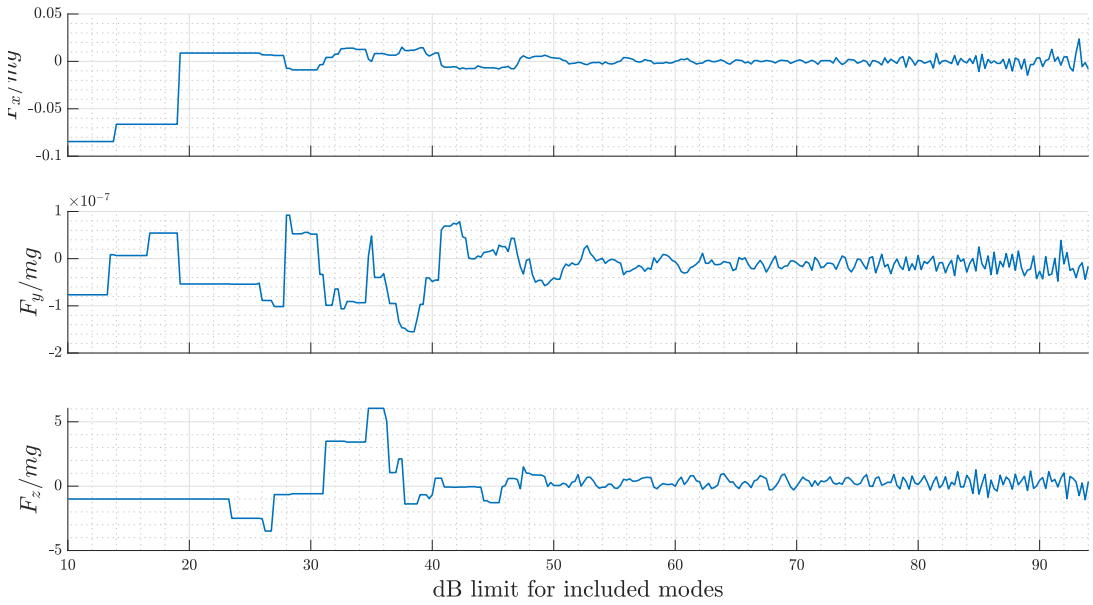

Figure B.1: Forces in x, y, and z direction at the center of trap 2, plotted over different dB limits for the selection of modes.

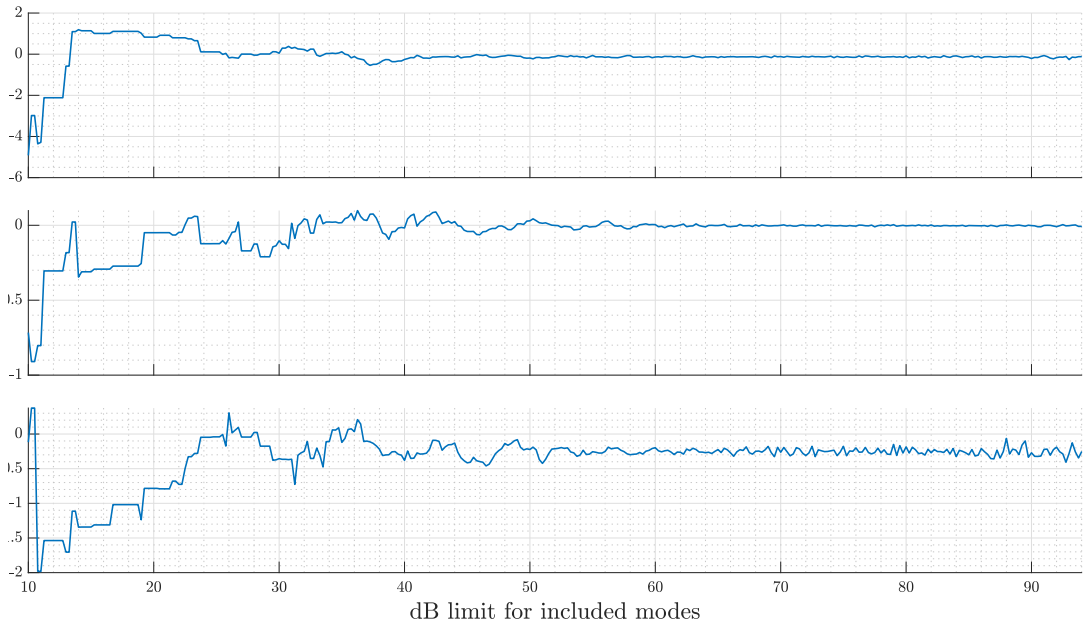

Figure B.2: Forces in x, y, and z direction at the center of trap 3, plotted over different dB limits for the selection of modes.

B.2 Simulated paths for experimentally found traps 1a and 1b

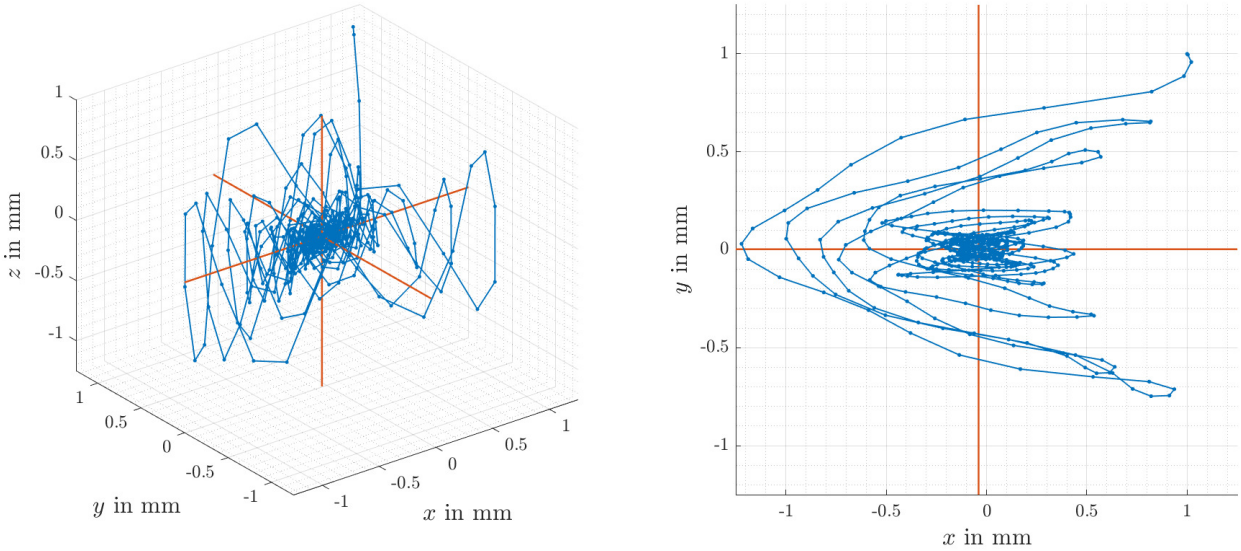

Figure B.3: Path simulation result for a bead placed near the experimentally found trap 1a, shown as a 3D plot to the left, and in the xy plane to the right.

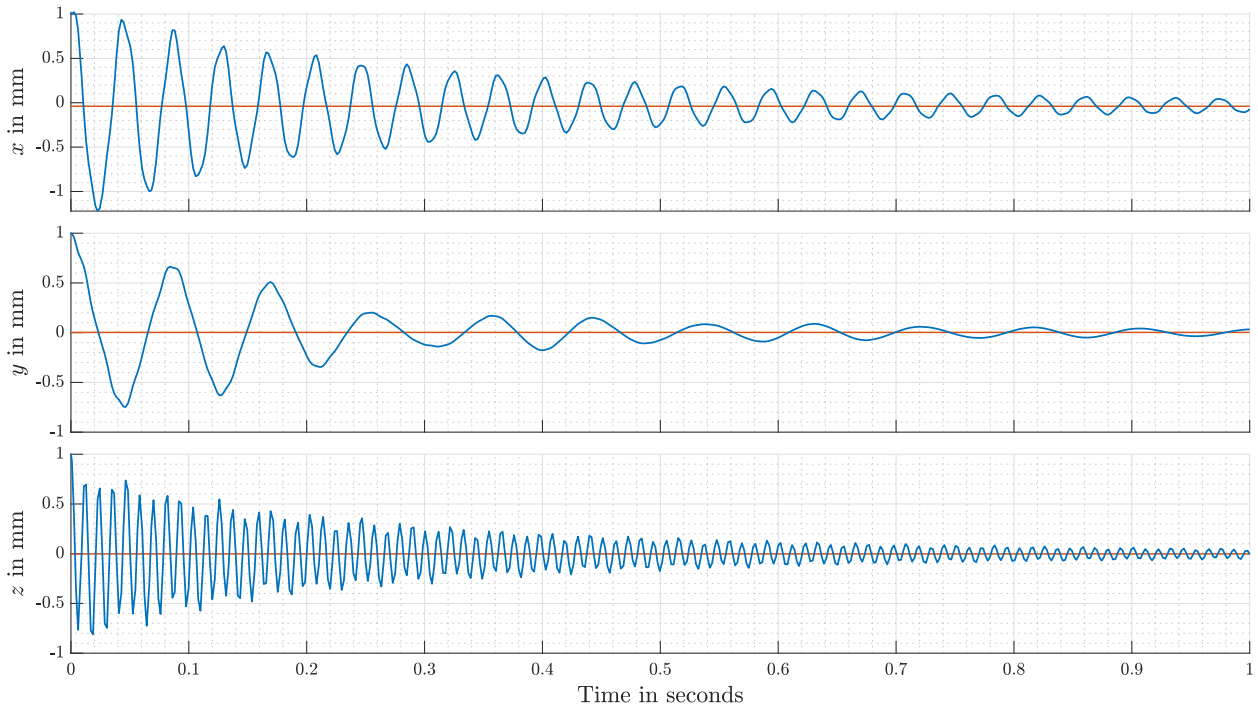

Figure B.4: Path simulation result for a bead placed near the experimentally found trap 1a, shown in x, y, and z coordinates individually.

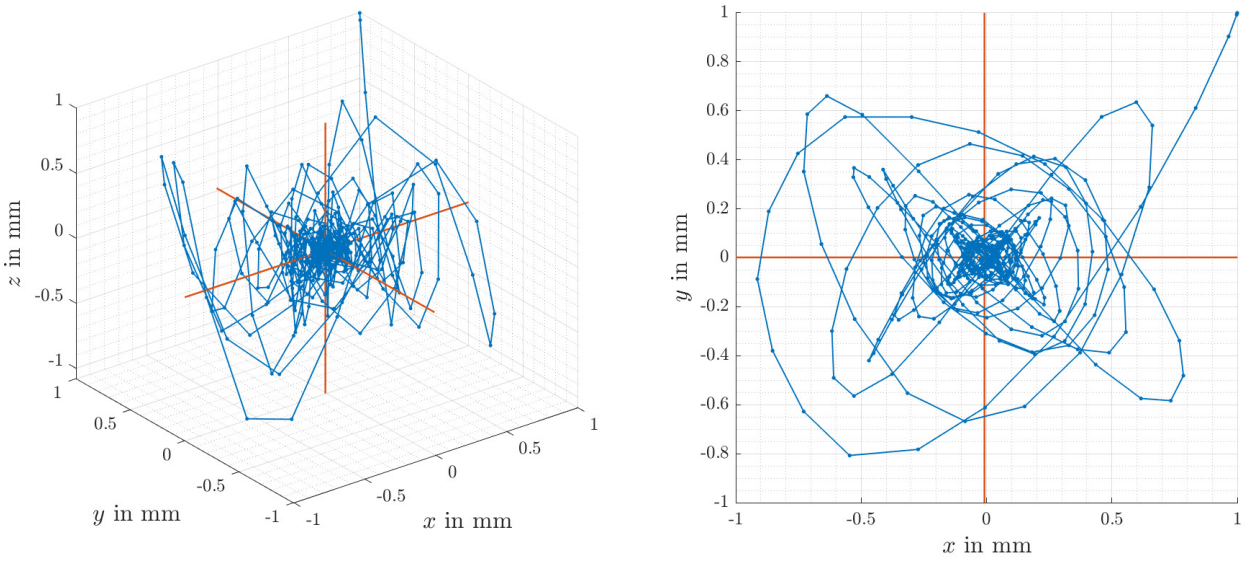

Figure B.5: Path simulation result for a bead placed near the experimentally found trap 1b, shown as a 3D plot to the left, and in the xy plane to the right.

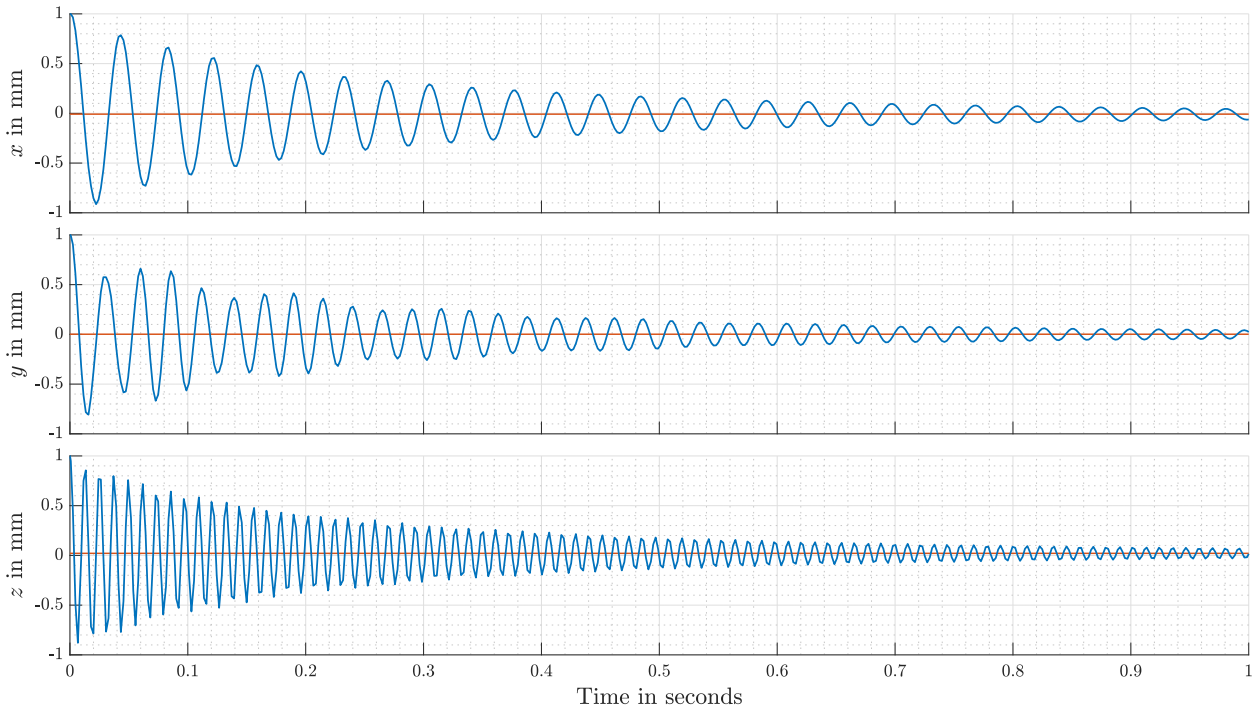

Figure B.6: Path simulation result for a bead placed near the experimentally found trap 1b, shown in x, y, and z coordinates individually.